THE JOURNAL OF PHYSICAL CHEMISTRY C
A JOURNAL OF THE AMERICAN CHEMICAL SOCIETY



pubs.acs.org/JPCC
Article

# Influence of the $CeO_2$ Morphology and Initial Pd–Pt Interaction Degree on Catalyst Activity and Stability

Andrea De Giacinto, Paolo Dolcet, Di Wang, Joachim Czechowsky, Carina B. Maliakkal, Christian Kübel, Silke Behrens, Jan-Dierk Grunwaldt, Silvia Gross,* and Maria Casapu*

Cite This: https://doi.org/10.1021/acs.jpcc.5c04366
Read Online



**ABSTRACT:** Due to its peculiar properties and strong interaction with noble metals, ceria is widely used as a catalyst support for numerous applications. In this work, morphologically pure and highly crystalline ceria nanocubes and nanorods were prepared to systematically investigate both the impact of the support morphology and Pd–Pt interaction degree on the noble metal-support interplay during CO oxidation. By using a constant surface noble metal concentration, the same probability for cluster/nanoparticle formation or noble metal redispersion during catalyst pretreatment and under reaction conditions was ensured. This novel approach allows for highlighting the impact of the support morphology on the catalyst dynamics and reveals different activity trends compared to what was previously reported for monometallic Pd- or Pt-catalysts supported on $CeO_2$. In particular, complementary *ex situ* and *in situ*/*operando* characterization tools combined with catalytic tests uncovered that by tuning the morphology and surface characteristics of ceria, the clustering and redispersion of the deposited noble metals in different atmospheres (e.g., oxidizing/reducing) can be controlled. The initial state and corresponding catalyst dynamics were thoroughly probed, showing that by depositing Pt and Pd on $CeO_2$-nanocubes, a balanced noble metal–support interaction is obtained that promotes the formation and retention of small and active noble metal clusters, regardless of the initial Pd–Pt interaction. In contrast, a high number of surface defects, as evidenced by Raman spectroscopy for $CeO_2$-nanorods, fosters the formation of highly dispersed species with a decreased low-temperature activity. Pd and Pt species with minimal mutual interaction performed better during CO oxidation, while the presence of alloyed particles on ceria prevented rapid noble metal redispersion and thus catalyst deactivation. Based on a rational adjustment of the noble metal–support interaction, the findings of this study are expected to contribute to the future development of NM/$CeO_2$-based catalysts containing the desired active sites, i.e., highly dispersed species or nanoparticles.

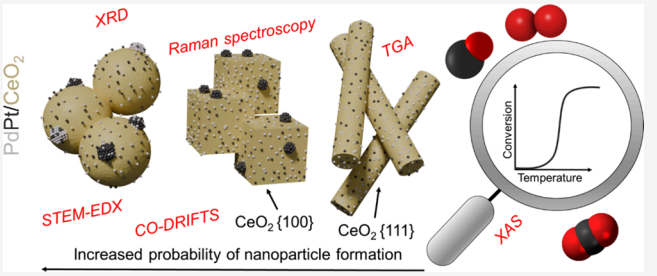


## 1. INTRODUCTION

During the last decades, the interaction between the platinum group metals and reducible metal oxide carriers such as $CeO_2$ has been exploited for various catalytic applications[1,2] including emission control,[3,4] fine chemistry, electrocatalysis, or energy-related processes.[5] Particularly, ceria plays a critical role in the activity, selectivity, and stability of the catalysts.[6−8] Its behavior directly depends on several structural characteristics including: porosity,[9,10] reducibility of the surface and bulk,[11−13] morphology/exposed facets,[14,15] and the interplay with the noble metals (NM) nanoparticles (NPs).[16,17] Herein, the strong noble metal–support interaction[18−20] is reported to tremendously affect the activity profile as well as the dynamics of various catalytic systems under reaction conditions.[7,17,21] While redispersion and particle formation phenomena have been observed for both Pt and Pd depending on the gas atmosphere and temperature of a certain pretreatment procedure,[16,22,23] the noble metal support interaction slightly varies for the two noble metals. As shown by Gashnikova *et al.*,[24] the diffusion barrier of Pd single sites on the $CeO_2$(111) surface is lower in comparison to that calculated for the corresponding Pt species. Studies on Pd-based catalysts supported on differently shaped $CeO_2$ reported the influence of the NM particle size, which affects the length of the metal-ceria interface,[25] on the catalyst reactivity. Further studies on monometallic Pd-[26,27] or Pt-based[28,29] catalysts linked the stability of isolated noble metal species or nanoparticles to the different ceria morphologies, i.e., different exposed facets. In the study of Spezzati *et al.*,[30] Pd NPs supported on ceria rods with (111) facets and ceria cubes exposing mainly (100) facets were spectroscopically investigated to elucidate the observed CO oxidation trends. The authors assigned different reaction mechanisms depending on the ceria morphology, i.e.,

Received: June 24, 2025
Revised: July 17, 2025
Accepted: July 17, 2025

Langmuir−Hinshelwood for the catalyst supported on $CeO_2$-rods and Mars−van Krevelen for the one supported on $CeO_2$-cubes. In contrast, Hu *et al.*[31] related the CO oxidation activity to the catalyst reducibility and oxygen vacancies formation, which was evaluated by Raman spectroscopy as a commonly applied characterization method for ceria-based materials.[32] The catalytic activity followed the order: $Pd/CeO_2$-rods > $Pd/CeO_2$-cubes > $Pd/CeO_2$-octahedra. Analogously, several studies have been published for $Pt/CeO_2$ catalysts supported on different $CeO_2$ morphologies.[15,33−35] The general catalytic activity trend is very similar to that observed for the Pd-catalyst series: $Pt/CeO_2$-rods > $Pt/CeO_2$-cubes > $Pt/CeO_2$-polyhedral.[15,33,34] However, in many cases, the role of the surface noble metal concentration (SNMC) and of catalyst pretreatment has been underestimated. Pretreatment in a reductive atmosphere (e.g., $H_2$, CO) might lead to increased activity due to the partial reduction of noble metal species.[16] Moreover, most of the investigations reported so far[15,30,31,34] compared $CeO_2$ supports having a different specific surface area (SSA) but loaded with the same NM amount. If the same NM loading is used for $CeO_2$ supports with different SSA, the premises for NM clusters/particle formation under reaction conditions, which are dependent on the spatial proximity of NM species, are not equivalent. As the onset of an oxidation reaction was shown to be directly affected by the probability of *in situ* NM clusters/particles formation,[22,36,37] using the same NM loading for different $CeO_2$ morphologies will result in activity trends affected by the variations in the SNMC while the impact of the support morphology is at least partially masked. Furthermore, in the previous studies comparing monometallic systems containing different noble metals, typically, the same sample mass and NM wt % loading were employed for the catalytic tests irrespective of the NM type and its molar mass. Considering that the compared catalysts contained different numbers of active species, the obtained trends in activity require a more accurate evaluation.

Since the nanostructured supports are highly sensitive to the reaction conditions, i.e., temperature and pretreatment conditions, special care needs to be taken to accurately assign their catalytic performance. For instance, pretreatments at lower temperatures than those applied during the catalytic tests[34] can subsequently lead to pronounced structural changes depending on the gas atmosphere applied, while high-temperature treatments (above 500 °C) can severely affect the properties (e.g., SSA, exposed facets, sharp edges) of the nanostructured support.[35] Regarding this aspect, $CeO_2$ nanocrystals are known to undergo reconstruction at high temperatures to minimize the surface energy. Herein, the (111) facet has been reported to be the most stable, followed by (110) and (100) surfaces.[14] More recent studies have shown that this structural evolution is decelerated in the presence of NMs.[38]

Finally, for bimetallic catalysts on alumina, the interaction between Pd and Pt brings additional complexity to the catalytic system. Skoglundh *et al.*[39] showed that a lower light-off (LOff) temperature is obtained for oxidation reactions if a Pd:Pt ratio of 4:1 (molar) is applied for alumina-supported catalysts. On the same support, the addition of Pd was found to diminish the CO self-poisoning effect of Pt-based catalysts, and to prevent strong noble metal sintering at high temperatures.[40−42] Nevertheless, under reaction conditions, surface enrichment of bimetallic particles with Pd or Pt occurs depending on the Pd:Pt ratio. Moreover, segregation phenomena were reported to occur on alumina-based supports after long-term usage[43] or under dynamic reaction conditions.[44] On ceria-based supports, the strong noble metal−support interaction further impacts these processes. Already under stoichiometric reaction conditions, a pronounced evolution of the bimetallic particles has been recently reported on commercial $CeO_2$,[45] which is expected to be further amplified if $O_2$-rich gas atmospheres are applied. Finally, for other catalytic reactions, i.e., $CH_4$ oxidation, previous *in situ/operando* studies on ceria-based catalysts have revealed that Pt addition to Pd promotes the formation of a reduced Pd phase.[45−47]

In this context, we report a systematic study comparing bimetallic Pd−Pt CO oxidation catalysts supported on hydrothermally synthesized and morphologically pure $CeO_2$-nanocubes and nanorods. Two main research directions were considered to cover several possible states of bimetallic Pd−Pt/$CeO_2$ catalysts: (i) elucidate the effect of $CeO_2$ morphology, i.e., rods vs cubes, for weakly interacting Pd−Pt entities by using the same SNMC, and (ii) uncover the evolution and catalytic behavior of PdPt bimetallic entities in alloyed and unalloyed states on $CeO_2$ cubes under reaction conditions. To the best of our knowledge, no previous investigations involving *in situ/operando* characterization of PdPt bimetallic catalysts supported on different ceria morphologies have been published so far. A commercial ceria support was used as a reference for nonpreferential exposed facets and reduced defects/vacancies concentration. Preformed alloyed and unalloyed Pd−Pt entities were obtained through a colloidal synthesis and deposited on the ceria support via wet impregnation. To highlight the effect of the ceria morphology and decouple the SNMC influence, the total noble metal loading was normalized to the SSA of each different ceria support. In comparison to previous literature, this approach revealed different catalytic trends with respect to the $CeO_2$ morphology impact. In addition, the Pt precursor was changed to promote or prevent the Pd−Pt interaction during the synthesis. The complex metal−support interactions between Pd, Pt, and $CeO_2$ were then tracked during/after catalyst synthesis, pretreatment in oxidizing/reducing atmospheres, and under CO oxidation reaction conditions. Considering that the NM-$CeO_2$ interplay regulates the activity and stability of such systems, the trends observed in this study for CO oxidation can serve as guidelines for the rational development of more efficient Pd−Pt/$CeO_2$ catalysts for further reactions that occur under $O_2$-rich conditions.

## 2. EXPERIMENTAL SECTION

**2.1. Supports Synthesis.** The first type of $CeO_2$ ("-com") support was obtained by calcination of commercial ceria for 5 h at 700 °C in static air. As a second support, $CeO_2$-nanorods (-"rod") were synthesized by hydrothermally treating for 6 h at 100 °C an aqueous solution containing 0.1 M of $CeCl_3{\cdot}7H_2O$ and 9 M of NaOH, similarly as reported in a previous study.[48] As a third support, $CeO_2$-nanocubes (-"cub") were prepared by hydrothermally treating for 24 h at 200 °C a mixture of 0.07 M $CeNO_3{\cdot}6H_2O$ in an acetate buffer solution (1.46 M NaOAc, 2.12 M HAc) with 10 vol % EtOH, similarly as in ref 49. For both syntheses, the filling ratio of the Teflon liner was kept between 0.43 and 0.46. The resulting solid products and reaction solutions were transferred into plastic vials after cooling the reactor to room temperature, and centrifuged at 10,000 rpm for 5 min using a Z32-HK (Hermle) centrifuge. The obtained powders were washed 2 times with 15 mL of


https://doi.org/10.1021/acs.jpcc.5c04366
J. Phys. Chem. C XXXX, XXX, XXX−XXX

deionized water and one last time with 15 mL of ethanol. The centrifuged products were dried at 80 °C overnight.

**2.2. Nanoparticle Synthesis.** To prepare the series of Pd−Pt/$CeO_2$ catalysts with different interaction degrees between the noble metals, Pd-rich NPs and dispersed $Pt^{2+}$ species (-"MF1") or alloyed PdPt NPs (-"MF2") were prepared in two colloidal suspensions.[50] The suspensions were obtained *via* microfluidic synthesis, which involved the chemical reduction of Pd and Pt precursors by $NaBH_4$, employing polyvinyl alcohol (PVA) or polyvinylpyrrolidone (PVP) as stabilizing agents against aggregation. In both cases, the molar ratio between the moles of monomeric units of the polymer and the total moles of noble metals was 6, and the molar ratio Pd:Pt was 1.8, as the aim was to obtain a Pd:Pt weight ratio of 1. The resulting total concentration of the NMs (Pd + Pt) in the two obtained colloidal suspensions was 4 mM. The continuous flow synthesis was conducted in a previously in-house built setup,[51,52] capable of generating a continuous and pulsation-free flow of reactants at high flow rates (>20 mL/min) to a cyclone micromixer integrated into a microfluidic chip. To obtain Pd-rich NPs and highly dispersed Pt species on the ceria support, a first solution of Pd and Pt precursors (-"MF1") was obtained by dissolving the appropriate amounts of $Pd(NO_3)_2{\cdot}2H_2O$ and $Pt(NH_3)_4(NO_3)_2$ precursors, together with PVA ($M_w$ = 9000−10,000) in deionized water. For the synthesis of Pd−Pt alloyed NPs, a second solution of $Pd(NO_3)_2{\cdot}2H_2O$ in deionized water and $H_2Pt(OH)_6$ dissolved in ice-cooled nitric acid was prepared (-"MF2") and mixed together with PVP ($M_w$ = 30,000). This method produced $Pt^{4+}$-nitrate species, which resulted in a more uniform reduction of the two metal species[53,54] and allowed for promotion of the Pd−Pt intermixing during the synthesis. In both cases, a solution of the reducing agent was obtained by adding the same amount of polymer in deionized water, which was followed by the addition of $NaBH_4$ and $HNO_3$ under mild stirring. The amount of $NaBH_4$ employed corresponds to 5 times the excess of the stoichiometric amount with respect to the total of noble metals.

**2.3. Supported Catalyst Preparation.** For the series of Pd−Pt bimetallic catalysts, the wet impregnation of the NMs suspension onto the supports was performed using a Chemspeed Accelerator SLT 106163.[55] To ensure the same SNMC, the total loading of Pd and Pt was adjusted as a function of the SSA of each $CeO_2$ support used in this study, aiming for a loading of $2.510^{-4}$ $g_{(Pd+Pt)}/m^2$. While maintaining a Pd:Pt molar ratio of ∼2, a total NM loading varying between ∼0.3−1 wt % for Pt and 0.3−0.8 wt % for Pd was selected. These values ensure the formation of small NM entities with a high number of exposed sites while providing sufficient NM loading for obtaining a reasonable quality of the data during the *operando* XAS measurements. After the impregnation, the powders were dried in vacuum at 60 °C. After completing the impregnation of the powders, the obtained Pd−Pt bimetallic catalysts were removed from the reactors, placed in crucibles, and calcined in static air at 500 °C for 1 h with a heating ramp of 10 °C/min, to completely remove the residues deriving from the NPs synthesis. Additional information on the selection of this procedure is provided by the TG-MS analysis during a simulated calcination step (temperature-programmed oxidation/TPO), which is shown in Figure S1. The resulting samples are from now on referred to as "fresh".

Reference Pd and Pt monometallic catalysts were prepared by incipient wetness impregnation (IWI) of aqueous solutions of $Pd(NH_3)_4(NO_3)_2$ and $Pt(NH_3)_4(NO_3)_2$ precursors on the commercial $CeO_2$ support, in line with the procedure described in the previous literature.[16,36,37] The selection of the monometallic reference samples was done with the aim of minimizing the number of structural parameters that could influence the CO oxidation activity. Taking a commercial $CeO_2$ and a conventional preparation method allows a direct comparison of these results with those obtained for well-understood NM-$CeO_2$-based catalysts. Such systems are characterized in detail in literature[12,36,56,57] and known to contain homogeneously distributed and highly dispersed NM species. The resulting samples were dried overnight at 80 °C and calcined in static air at 500 °C for 1 h with a heating ramp of 10 °C/min. The desired noble metal loading was adjusted to the specific surface area of the support, as for the previously described samples.

For the discussion of the results, the three Pd−Pt bimetallic samples obtained by using the MF1 suspension of noble metal species will be labeled as "PdPt-MF1-xxx", where xxx denotes the morphology of $CeO_2$ impregnated support, i.e., "com" for commercial, "rod" for nanorods, and "cub" for nanocubes. The sample obtained by impregnation of $CeO_2$-nanocubes with the MF2 suspension is denoted as "PdPt-MF2-cub". The monometallic catalysts obtained by IWI of the commercial ceria support will be labeled as "Pd- IWI-com" and "Pt-IWI-com".

**2.4. Characterization Methods.** The elemental composition of the catalysts was determined via inductively coupled plasma optical emission spectrometry (ICP-OES) on an iCAP 7600 DUO (Thermo-Fisher-Scientific). Before the analysis, 30−40 mg of sample (accuracy ±0.05 mg) was mineralized in 4 mL of HCl, 4 mL of $H_2SO_4$, and 2 mL of $H_2O_2$ and heated to 250 °C for 12 h in a DAB-2 pressure digestion vessel (Berghof). The analysis of the elements was accomplished with four different calibration solutions, and Sc was used as an internal standard.

The specific surface area of the prepared samples was determined by $N_2$ physisorption at −196 °C according to the Brunauer−Emmett−Teller (BET) theory[58] using a multipoint measurement on a BELSORP-mini II instrument (BEL, Europe). Adsorption isotherms were evaluated in the range of $p/p_0$ = 0.05 to 0.3. The total pore volume of the samples was determined using the Barrett−Joyner−Halenda (BJH) method.[59] Before the analysis, the samples were degassed at 200 °C under reduced pressure on a BELPREP-vac II instrument (BEL, Europe) for 2 h.

The crystalline structure and phase purity of the synthesized nanostructured powders were determined by X-ray diffraction (XRD). XRD patterns were recorded using a D8 Advance (Bruker) diffractometer with CuK$\alpha$ radiation (wavelength = 1.5406 Å). Each measurement was performed in the $2\theta$ range 10°-120° with a step size of $2\theta$ = 0.017° and 10 s per step dwell time. The crystallite size was estimated from the average of 3 different reflections using the Scherrer equation (with $K$ = 0.94). For nanorods, the (111), (220), and (311) reflections of cubic ceria were used. For nanocubes and commercial ceria, the (111), (200), and (220) reflections were used.

To assess the thermal stability of the supports, scanning electron microscopy was performed using a GeminiSEM 500 (Zeiss) instrument equipped with a thermal Schottky field emitter cathode. The SEM was equipped with a retractable backscatter secondary electron detector with five segments. The InLens secondary electron detector and in-column energy-


https://doi.org/10.1021/acs.jpcc.5c04366
J. Phys. Chem. C XXXX, XXX, XXX−XXX

selective backscattered (EsB) detector could be used up to 150 Pa (NanoVP). Inside the chamber, an Everhart-Thornley secondary electron detector and a variable pressure secondary electron detector were mounted. The operating software employed was SmartSEM (version 6.01). For the quantitative analysis of micro areas and the elemental distribution, an energy-dispersive X-ray spectrometer X-MaxN (Oxford) with a silicon drift detector (size: 80 $mm^2$, resolution: 127 eV) was used. The software employed for data analysis was Aztec (version 3.3).

The nanostructured ceria supports (nanorods, nanocubes) were characterized on a Themis-Z double corrected transmission electron microscope (TEM) (Thermofisher Scientific) operated at 300 kV. Scanning transmission electron microscopy (STEM) images were acquired by using a high-angle annular dark-field (HAADF) detector. The impregnated catalyst PdPt-MF1-rod before calcination was characterized on a FEI Osiris ChemiSTEM microscope operated at 200 keV. The catalysts were characterized, in the fresh state and after the catalytic test run, on a probe-corrected Themis 300 TEM (Thermofisher Scientific) instrument operated at 300 kV. STEM and TEM images were acquired by using a HAADF-STEM detector and a Ceta 16 M camera. Energy dispersive X-ray spectroscopy (EDX) analysis was performed by using a Super-X EDXS detector both on the FEI Osiris and on the Themis 300. During EDX mapping, currents and dwell times were kept below 100 pA and 50 $\mu$s to avoid beam-induced noble metal migration and agglomeration.

Raman spectroscopy was performed with an inVia Reflex Spectrometer System (Renishaw) equipped with a frequency-doubled Nd:YAG laser (532 nm, 100 mW at the source) and an optical microscope (Leica). Typically, the data was collected in a spectral range from 100 to 1300 $cm^{-1}$, with a resolution of ca. 1 $cm^{-1}$ by means of a 2400 lines/mm grating. A 50× objective was used to focus the laser. For each measurement point, 5 accumulations were collected. The laser power was set to 5% and the acquisition time was adjusted from 10 to 300 s, to have a comparable S/N ratio between different samples. Data treatment (e.g., background subtraction, normalization) was done with the WiRE 4.4 software (Renishaw). Oxygen deficits ($\delta$ in $CeO_{2-\delta}$) related to oxygen vacancy concentrations were estimated based on the shift of the main $F_{2g}$ band located around 460 $cm^{-1}$ for pure $CeO_2$. As applied in previous studies,[60] the relation between the crystallite volume change ($\Delta V$) and the frequency shift $\Delta\omega = -\gamma\omega/(\Delta V/V_0)$ ($\Delta\omega$—the shift in Raman frequency, $\gamma$—the Grüneisen parameter) was used, considering as reference frequency the value measured for the calcined commercial $CeO_2$. Considering the linearity between the changes in oxygen deficit $\delta$ and the change in volume $\Delta V/V_0$, the oxygen deficits related to oxygen vacancies were calculated using the relation $\delta = 2.66(\Delta\omega/\omega)$.

The redox properties of the bare $CeO_2$ supports and of the final catalysts were studied by thermogravimetric analysis on a simultaneous thermal analyzer (STA 449 F3 Jupiter, NETZSCH), with a resolution of 0.1 $\mu$g. The instrument is coupled to a quadrupole mass spectrometer (QMS 403 Aëolos Quadro, NETZSCH) for the detection of the evolved gases. 50 ± 0.5 mg of powdered sample was placed in a crucible and introduced into the furnace. The analysis protocol was divided into two subsequent experiments at 100 mL/min gas flow and 5 °C/min ramp rate: at first, a temperature-programmed oxidation (TPO) was performed in 10 vol % $O_2$/Ar, followed by a temperature-programmed reduction (TPR) in 5 vol % $H_2$/Ar up to 500 °C.

Diffuse reflectance infrared Fourier transform spectroscopy (DRIFTS) measurements were performed on a VERTEX 70 Fourier transform infrared spectrometer (Bruker) equipped with Praying Mantis diffuse reflection optics (Harrick) and a liquid-nitrogen-cooled mercury cadmium telluride (MCD) detector. For the DRIFTS measurements, the catalyst was pressed and sieved at the desired sieve fraction (100−200 $\mu$m). The catalyst bed was prepared by filling part of the sample holder with ∼150 mg of $CaF_2$ (sieve fraction 100−200 $\mu$m). On top, a layer of catalyst sieved fraction (∼50 mg) was placed. A *in situ* cell (Harrick) covered with a $CaF_2$ window was used to collect DRIFTS spectra. The temperature in the reactor was controlled by two heating cartridges inside the cell and a water-cooling system. The gas flow at all stages of the experiment was 100 mL/min. Before dosing the reaction mixture and proceeding with the experiments, the catalysts were pretreated at 350 °C for 30 min in 10% $O_2$/Ar at ambient pressure. Afterward, the cell was cooled to room temperature (30 °C) in Ar, where a background spectrum (catalyst in a completely oxidized state without having seen CO) was recorded. The recorded spectra (4 $cm^{-1}$ resolution; 300 accumulations per spectrum, 30 °C) were converted to pseudoabsorbance by calculating the negative logarithm of the ratio between the spectrum of the sample and the background spectrum. CO adsorption was performed in the reaction mixture (1000 ppm of CO, 10%$O_2$, Ar rest), as employed during the catalytic tests for preventing a significant change of the sample and minimize the interference of the gas phase CO.[22,61,62] CO adsorption was performed before and after heating and cooling the catalyst in the reaction mixture to 300 °C. This procedure was repeated after a reductive treatment for 30 min at 300 °C in 5%$H_2$/Ar, and after cooling the catalyst bed in Ar to room temperature. Background subtraction and peak deconvolution into Gaussian peaks were performed using the Origin software.

*In situ* and *operando* X-ray absorption spectroscopy (XAS) measurements at the Pd K edge (24,350 eV) and Pt $L_3$ edge (11,564 eV) for the PdPt-MF1 series were performed at the BM23 beamline[63] of the European Synchrotron Radiation Facility (ESRF). A Si(111) crystal monochromator was used for energy selection at the Pt $L_3$ edge, while at the Pd K edge, a Si(311) double crystal monochromator was used. The X-ray beam size was adjusted down to 80 × 1000 $\mu m^2$, and the data were collected in fluorescence mode using a one-element Vortex Silicon Drift Detector (SDD), model EX90 (Hitechi High-Technologies Science America, Inc.). *In situ* XANES spectra were recorded with an acquisition rate of ∼3 min/scan as a function of time and temperature (ca. one spectrum every 30 °C) during $H_2$-TPR and CO oxidation experiments.

The PdPt-MF2-cub sample was investigated at the SAMBA beamline[64] of the SOLEIL synchrotron during catalyst pretreatment and CO oxidation. Si(220) channel-cut crystals were used for the measurements at the Pt $L_3$ edge and Pd K edge. The X-ray beam size was set to 200 × 1500 $\mu m^2$. XAS data were collected in fluorescence mode using a 35-pixel HPGe fluorescence detector (Canberra). *In situ* XANES spectra were recorded with an acquisition rate of ∼2.5 min/scan as a function of time and temperature (ca. one spectrum every 25 °C) during $H_2$-TPR and CO oxidation experiments.

A quartz capillary microreactor (inner diameter = 1.48 mm, wall thickness 20 $\mu$m) was used as an *in situ*/*operando* cell,[65]


https://doi.org/10.1021/acs.jpcc.5c04366
J. Phys. Chem. C XXXX, XXX, XXX−XXX

and heated with a hot air gas blower (Oxford) at a heating ramp of 10 °C/min. The microreactor was loaded with the granulated catalysts (100−200 μm mesh), inserting the adequate amount to reach a constant weight hourly space velocity (WHSV) of 60,000 $L{\cdot}g^{-1}_{Pd+Pt}{\cdot}h^{-1}$. The total gas flow, containing 5 vol % $H_2$/He for reduction or 1000 ppm of CO, 10 vol % $O_2$ in He for CO oxidation, was set to 70 mL/min via mass flow controllers (Bruker). The gas concentration in the product flow was monitored online using an AO2000 Series (ABB Automation GmbH) nondispersive infrared analyzer and a mass spectrometer (Omnistar, Pfeiffer Vacuum). Additional *ex situ* XAS measurements were conducted at the SAMBA beamline of the SOLEIL synchrotron. The obtained XAS data were deglitched, normalized, and background-subtracted using the Demeter software package.[66] The normalized XANES spectra were evaluated by linear combination analysis (LCA) within the region −30 to +50 eV. The spectra of a $PtO_2$ pellet and of a metallic Pt foil were used as references for the linear combination analysis (LCA) of all transmission data and fluorescence at the Pt $L_3$ edge. For Pd K edge XAS data collected in fluorescence mode, the spectra of known well-characterized nanoparticle samples in their highest oxidation state (after oxidation at 500 °C in air) and lowest oxidation state (after reduction at 300 °C in 5 vol % $H_2$/He) were used as reference spectra for LCA.

During the *operando* XAS experiment, 15 spectra were collected at room temperature in fluorescence mode at different stages of the experiment and were merged and used for the EXAFS fitting. A *k*-range of 3−10 $Å^{-1}$ was employed while the fitting of the Fourier transform EXAFS (FT-EXAFS) data was performed in the *R*-range of 1.0−3.0 Å using the software Artemis from the Demeter software package.[66] The number of independent points resulting from the *k*- and *R*-ranges during the EXAFS fitting was 8; thus, the number of variables was limited to 7. Due to the complex catalyst structure containing several phases (alloyed/mixed particles and highly dispersed species in different oxidation states), several models were used during the fitting procedure. For fitting the structure of metallic PdPt alloys and $Pd_{0.5}Pt_{0.5}O$ oxide, the coordination paths were adapted based on pure Pd and PdO. Pd atoms surrounding the central Pd atom were exchanged by Pt, and the distance between atoms was adjusted assuming a stoichiometric 1:1 mixture, i.e., the mean value of the distance in Pd and Pt for the metallic structure and of PdO and PtO for the oxide. To simulate highly dispersed Pd-atoms, a DFT calculated $Pd/CeO_2(111)$ model of $CeO_2(111)$ substituted $Pd^{2+}$ single sites proposed by Gashnikova *et al.*[37] was used. Details on the fitting procedure are provided in Tables S4 and S5.

**2.5. Catalytic Tests.** Analogous to the *operando* XAS measurements, the catalytic performance of the different Pd−Pt samples was evaluated in a quartz capillary plug-flow reactor (outer diameter = 1.5 mm; wall thickness 20 μm) heated with a hot air gas blower (Oxford). EL-FLOW Select (Bronkhorst) MFCs and stainless-steel piping lines were used to dose the gases (He, $O_2$, $H_2$, and CO) into the reactor. The CO and $CO_2$ concentrations in the product flow were monitored online with an FTIR instrument (MultiGas 2030 FTIR Continuous Gas Analyzer, MKS Instruments). The error in the determination of the CO concentration with the FTIR analyzer is below 5 ppm; therefore, the final error on the conversion value is below 2%. The amount of sample loaded (100−200 μm mesh) in the microreactor was adjusted to obtain a WHSV of 60,000 $L{\cdot}g^{-1}_{Pd+Pt}{\cdot}h^{-1}$ (GHSV, ∼500,000 $h^{-1}$ at standard conditions) at a total gas flow of 70 mL/min. Three light-off/light-out (LOff/LOut) cycles in reaction mixture (1000 ppm of CO, 10 vol % $O_2$ and He as balance) were carried out for the fresh catalyst while heating/cooling the catalytic bed from 25 to 300 °C. In between the ramps, the catalyst was held at 25 and 300 °C for 10 min. In the next step, the catalyst was reduced in 5 vol % $H_2$/He at 300 °C for 30 min. After reduction, the sample was cooled down in He to avoid the formation of Pd hydrides.[67] In a next step, three additional CO oxidation LOff/LOut cycles were performed to evaluate the activity of the sample after prereduction. All of the heating and cooling ramps were performed at 10 °C/min. In general, the catalyst testing procedure, i.e., transient conditions and gas concentrations, was selected to mimic $O_2$-rich conditions that are present in the exhaust of lean combustion engines. Several LOff/LOut cycles were conducted to observe the effect of the initial catalyst structure on the activity profile and also to identify dynamic structural changes and their effect on the catalyst performance.

## 3. RESULTS AND DISCUSSION

**3.1. Material Characterization.** By carefully adjusting the hydrothermal and solvothermal synthesis methods, $CeO_2$ nanostructures with defined morphology, preferred surface orientation, and narrow size distribution were obtained (Figures 1 and S2). Based on the HAADF-STEM character-

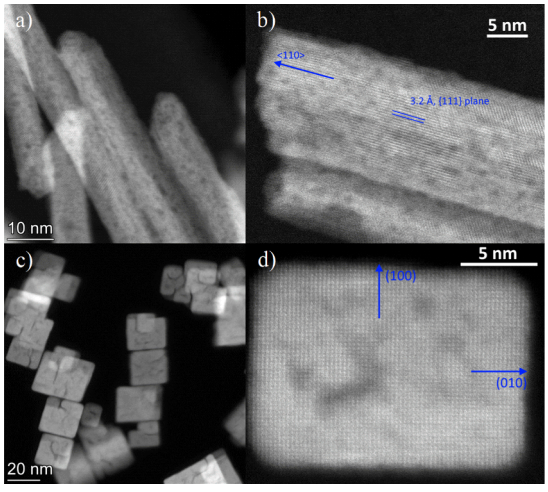


**Figure 1.** HAADF-STEM images of the ceria nanorods (a, b) and nanocubes (c, d) supports.

ization, the derived average length and width of the nanorods were 80 ± 4 and 10.6 ± 0.3 nm, respectively, with an average aspect ratio of 7.5 ± 0.3. These results, together with the average crystallite size of 6.0 ± 1.0 nm estimated from the XRD patterns using the Scherrer equation[68] (details on the calculation are provided in the SI, Figure S3 and Table S1), confirm the polycrystallinity reported for rods synthesized under similar conditions.[48] The darker patches visible in Figure 1a,b correspond to the depletion of material and hint toward a porous network inside the rods.[69,70] Assuming a hexagonal section[69] and flat nonporous surfaces, the measured dimensions of the nanorods would result in a specific surface area of 65 $m^2/g$. The discrepancy in the BET-determined surface area of 108 $m^2/g$ (Table 1) further confirms the porosity of the nanorods. Overall, the measured SSA is slightly


https://doi.org/10.1021/acs.jpcc.5c04366
J. Phys. Chem. C XXXX, XXX, XXX−XXX

Table 1. Characterization Results Derived from the $N_2$ Physisorption Measurements and ICP-OES Analysis

| sample | SSA ($m^2/g$)[a] | nominal loading (wt %)[b] | ICP-OES (wt %)[b] | Pd:Pt (wt) | Pd:Pt (at) | SNMC[c] ($g_{(Pd+Pt)}/m^2$) |
|---|---|---|---|---|---|---|
| PdPt-MF1-com | 85 | 2.1 | 1.60 | 0.80 | 1.46 | $1.9 \cdot 10^{-4}$ |
| PdPt- MF1-rod | 108 | 2.7 | 1.88 | 0.80 | 1.47 | $1.7 \cdot 10^{-4}$ |
| PdPt- MF1-cub | 35 | 0.9 | 0.58 | 0.77 | 1.41 | $1.6 \cdot 10^{-4}$ |
| PdPt- MF2-cub | 40 | 1.0 | 0.87 | 1.00 | 1.82 | $2.1 \cdot 10^{-4}$ |
| Pd-IWI-com | 85 | 2.1 | 1.86 | | | $2.2 \cdot 10^{-4}$ |
| Pt-IWI-com | 85 | 2.1 | | | | $2.5 \cdot 10^{-4}$[d] |

[a]Evaluated using the BET method. [b]Refers to the sum of Pd and Pt wt % loadings. [c]Target SNMC was $2.5 \cdot 10^{-4}$ $g_{(Pd+Pt)}/m^2$. [d]Calculated based on the nominal loading.

higher than the range reported in the literature for $CeO_2$-nanorods synthesized by analogous procedures.[15,31,34,71,72] Based on a large number of high-resolution STEM images, lattice planes parallel to the rod axis could be identified. Therefore, the rod axis direction was determined to be ⟨110⟩. In previous studies with the same long axis direction, the main exposed side surfaces were composed of (111) facets.[30,71]

Based on HAADF-STEM characterization, an average edge length of 21.9 ± 0.6 nm was obtained for $CeO_2$-nanocubes (additional information in Figure S2), which aligns with the average crystallite size of 24.1 ± 1.2 nm calculated from the XRD data using the Scherrer equation.[68] This similarity and the uniform lattice structure in the HAADF-STEM images point toward the formation of single-crystalline nanocubes. Sharp edges and low truncation result in a small amount of (111) and (110) facets[69] being exposed. A theoretical SSA value of 38 $m^2/g$ was derived based on edge length measured from the TEM micrographs, assuming flat surfaces. The SSA was further estimated by nitrogen physisorption, and a value of about 35 $m^2/g$ (Table 1) was obtained, which is similar to that reported by Lyu *et al.*[49] Both $CeO_2$ morphologies were preserved after the impregnation with the colloidal suspension of NM NPs (Figure S4) and the calcination step (Figure 2). Further SEM-EDX analysis (Figures S5 and S6) confirmed the good thermal stability of the pure $CeO_2$ nanostructures up to 500 °C. Nevertheless, while the thermal treatment at 500 °C is suitable for the evaluation of the CO oxidation activity over Pd−Pt/$CeO_2$ bimetallic systems, additional thermal aging investigations are necessary if the application of these catalysts is considered for reactions occurring at higher temperatures, e.g., $CH_4$ oxidation. Additionally, the presence of low Na traces was observed, a residue of the synthesis procedures. Furthermore, electron microscopy characterization (Figure S7) of the commercial ceria support with a surface area of 85 $m^2/g$ and of the corresponding PdPt-MF1-com catalyst confirmed the presence of polyhedral $CeO_2$ NPs (<20 nm) in this sample. The average $CeO_2$ crystallite size calculated with the Scherrer equation was 11.8 ± 1.2 nm, indicating an intermediate crystallite size between the rod- and cube-shaped supports. As described in the experimental section, bimetallic catalysts with either a poor or strong interaction between Pt and Pd were synthesized in this study by varying the Pt precursor. Due to the different reduction potentials of the $Pt^{2+}$- and $Pt^{4+}$-based precursors, the Pd−Pt coreduction process could be tuned[73] to stimulate or prevent the alloy formation. In this way, in addition to the effect of $CeO_2$ morphology, the influence of the Pd−Pt alloying degree on the CO oxidation activity and catalyst stability could be systematically evaluated. In line with the applied preparation procedures, the nominal total (Pd + Pt) NM loadings of the fresh catalysts determined by ICP-OES measurements are between 0.7−2.2 wt % for the

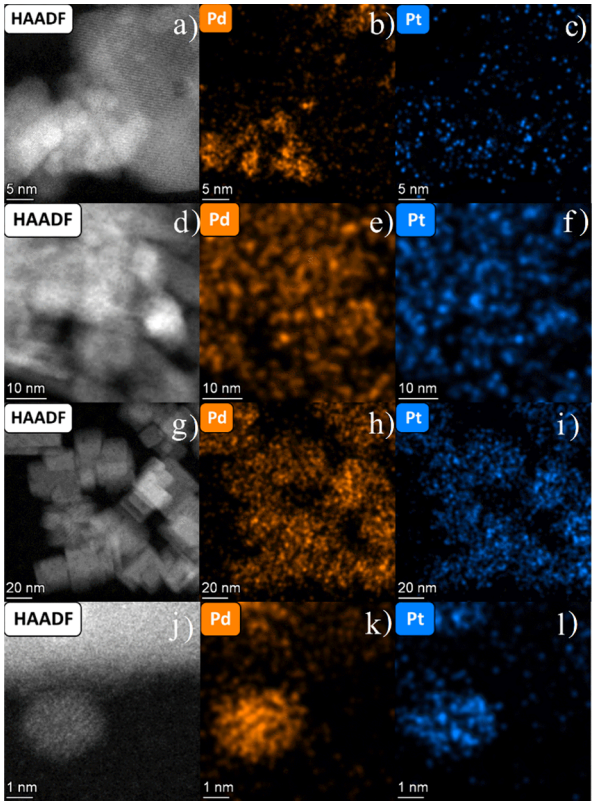


**Figure 2.** HAADF-STEM images of the fresh PdPt bimetallic catalysts, namely, PdPt-MF1-com (a), PdPt-MF1-rod (d), PdPt-MF1-cub (g), and PdPt-MF2-cub (j). EDX elemental mapping for Pd (b, e, h, k) and Pt (c, d, i, l) corresponding to the HAADF-STEM images.

different samples, with a Pd:Pt molar ratio of 1.5 for the bimetallic ones. These values correspond to a similar NM concentration per support surface area unit ($1.6–2.2 \cdot 10^{-4}$ $g_{(Pd+Pt)}/m^2$) for all samples, despite their different SSA. In this way, it was ensured that surface phenomena, such as the NM redispersion or the formation of NPs[36] during the sample pretreatment (i.e., calcination, reduction) and under reaction conditions,[62] were only affected by the different interactions with the exposed $CeO_2$ facets (for the MF1 series) or by the different interplay between Pd and Pt (bimetallic MF2 vs MF1 catalysts on $CeO_2$-nanocubes). Only for the PdPt-MF2-cub catalyst, a positive deviation of 20% in the NM loading and 30% in the Pd:Pt ratio (at) was identified.

According to the HAADF-STEM investigations and EDXS analysis of the impregnated PdPt-MF1-rod catalyst, the microfluidic synthesis protocol led to the formation of Pd-rich NPs with a narrow size distribution and an average size of 2.40 ± 0.05 nm (Figure S4). The EDXS quantification carried


https://doi.org/10.1021/acs.jpcc.5c04366
J. Phys. Chem. C XXXX, XXX, XXX−XXX

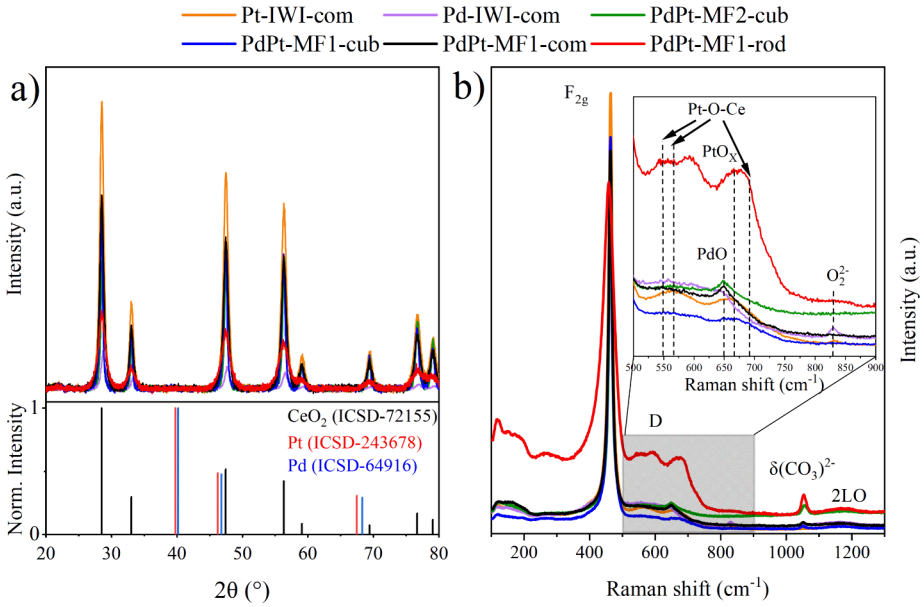


**Figure 3.** (a) XRD patterns ($\lambda$ = 1.5406 Å) and (b) Raman spectra ($\lambda_{exc}$ = 532 nm, region 100−1300 $cm^{-1}$) of the fresh catalysts. Inset in (b): 500−900 $cm^{-1}$ region with identified Pd- and Pt-related species. An additional enlarged image of the inset in part b is available in ESI (Figure S10).

out on isolated NPs revealed an average Pd:Pt molar ratio of ∼20:1 (quantification results are available as ESI, Table S2). This value indicates that most of the initially loaded Pt is distributed as highly dispersed species on the $CeO_2$ surface. This outcome of the synthesis procedure (MF1) is caused by the formation of $Pt^{2+}$-intermediates that are not efficiently reduced in the presence of $NaBH_4$, as previously reported by several research groups.[74−76] In contrast, by using a $Pt^{4+}$ precursor during the microfluidic synthesis (MF2), a suspension of alloyed Pd−Pt NPs was obtained. As illustrated in Figure 2 by the STEM-EDX characterization, in the fresh PdPt-MF2-cub sample, alloyed Pd−Pt particles with a mean size of 2.8 ± 0.7 nm are present. From the corresponding EDXS quantification on a relatively low number of particles, an average Pd:Pt molar ratio of 2.75 ± 0.25 was calculated. On the other hand, for the MF1 catalyst series, differences in the NM dispersion were noticed after calcination for 1 h at 500 °C. While the presence of subnanometer NM clusters was identified on ceria nanocubes and nanorods (Figure 2d−i), the catalyst supported on the commercial $CeO_2$ contains small NM clusters together with a few Pd-rich (Figure 2a−c) or Pt-rich particles/agglomerates (additional information in ESI, Figure S8). This outcome suggests a clear impact of the ceria morphology and the exposed $CeO_2$ facets on the interaction with the noble metal during the calcination step. Due to the low contrast, the Pd and Pt species could be visualized only by EDXS mapping, and the particle size distribution could not be precisely derived for PdPt-MF1-rod and PdPt-MF1-cub samples. In contrast, for the catalyst containing preformed Pd−Pt alloyed nanoparticles, the state is maintained after the calcination step.

Previous investigations showed that the stability of Pd NPs on ceria in an oxidative atmosphere is dependent on the support morphology, i.e., exposed facets and concentration of surface defects.[27] Furthermore, Ge *et al.*[77] showed that Pt-NPs with an average size of ∼2.4 nm on ceria rods and octahedra are stable during calcination at 400 °C. In contrast, Song *et al.*[29] revealed that for ultralow loaded $Pt/CeO_2$ catalysts on ceria rods and cubes that a higher stability for isolated Pt species is achieved on the former. Different adhesion energy was reported for Pt on ceria depending on the exposed facets. According to Eliasson *et al.*,[78] $Pt_{120}$ clusters/NPs seem to be more stable on ceria supports exposing the (111) facets compared to the ones exposing the (100) facets. Hence, while at temperatures above 500 °C complete redispersion of Pt and Pd and formation of isolated sites has been often reported in literature,[16,42,62] at low and moderate temperatures the redispersion kinetics seem to be more influenced by the $CeO_2$ surface characteristics.

XRD patterns were collected for all fresh catalysts, including the monometallic references (Figure 3a). In all cases, only characteristic reflections of the $CeO_2$ fluorite structure (ICSD-72155) were detected. The absence of Pd/Pt or $PdO/PtO_2$ reflections can be attributed to the small size (<3−4 nm) of NM species in all samples, as also indicated by the electron microscopy characterization. Furthermore, the characteristic ceria reflections visible in the XRD patterns of the fresh catalysts are narrower for the catalysts based on commercial $CeO_2$ and nanocubes compared to the one based on $CeO_2$-nanorods. This is a clear indication of the smaller crystallite size of the latter support and aligns well with the high porosity of the nanorods, as evidenced in Figure 1a,b. Figure 3b shows the Raman spectra of the different Pd−Pt/$CeO_2$ catalysts. In general, Raman spectroscopy is a widely applied technique to characterize ceria-based catalysts, including for the estimation of the oxygen vacancies and defects in commercial supports as well as in more defined ceria morphologies.[32,79] The main band appearing around 465 $cm^{-1}$ was previously attributed to the $F_{2g}$ vibrational mode of the $CeO_2$ fluorite phase.[32,80,81] The broadening of this intense peak has been correlated with an increased concentration of the oxygen vacancies and decreased size of $CeO_2$ nanocrystals.[80,82,83] Visual comparison of the Raman spectra obtained for the different $CeO_2$ supports suggests that the nanorod-based support (Figure S9) has the highest concentration of oxygen vacancies.[83] The same characteristic can be deduced from Figures 3b and S10 for the corresponding fresh PdPt- MF1-rod catalyst. This trend is confirmed by the quantitative evaluation of the oxygen


https://doi.org/10.1021/acs.jpcc.5c04366
J. Phys. Chem. C XXXX, XXX, XXX−XXX

vacancies for the different $CeO_2$ morphologies based on the observed Raman shift of the $F_{2g}$ band (Table 2). Furthermore,

**Table 2. Quantification of the Oxygen Deficit Based on the Raman shift of the $F_{2g}$ Band**

| sample | Raman shift/cm$^{-1}$ ($F_{2g}$) | oxygen deficit[a] |
|---|---|---|
| $CeO_2$ commercial | 465.3 | 0 |
| $CeO_2$ cubes | 463.8 | 0.009 |
| $CeO_2$ rods | 455.0 | 0.060 |
| PdPt-MF1-com | 463.6 | 0.010 |
| PdPt-MF1-cub | 463.6 | 0.010 |
| PdPt-MF1-rod | 458.3 | 0.041 |
| PdPt-MF2-cub | 464.1 | 0.007 |

[a]For the estimated ±0.3 cm$^{-1}$ uncertainty in $\Delta\omega/\omega$, the uncertainty in $\delta$ is ±0.002.

the broadening of the $F_{2g}$ band is in line with the smaller ceria crystallite size in the $CeO_2$-rods compared to that of the commercial- and nanocube-based $CeO_2$ supports and catalysts. Interestingly, for the rod-based samples, an additional band was recognized at around 596 cm$^{-1}$ (D-band), which was also previously associated with the presence of defects and oxygen vacancies in the ceria structure.[79,82,83] The insets of Figures 3b, S9, and S10 depict the features exhibited within this spectral region by the pure $CeO_2$ supports and Pd−Pt loaded catalysts. Raman band assignments based on literature are provided in Table S3. For pure ceria (Figure S9), these oxygen vacancies were assigned to intrinsic Frenkel anion pair defects caused by the movement of oxygen atoms into an octahedral interstitial position.[79] Additionally, the presence of reduced $Ce^{3+}$ cations was claimed to contribute to the formation of oxygen vacancies.[84,85] Nonetheless, this Raman band is not very visible for the other supports or catalysts, which is possibly due to the lower surface area of the nanocubes and the preliminary calcination step (5 h at 700 °C) employed to stabilize the commercial ceria support. Indeed, it is well-known that most of the oxygen vacancies in oxidized $CeO_2$ (the state of the fresh catalysts) are located on the surface, while the intensity of surface-related Raman bands is dependent on the SSA of the material.[1,32] On the other hand, the calcination of the commercial ceria might have promoted the exposure of the most thermodynamically stable (111) facet,[86−88] which has the highest activation energy for oxygen vacancy formation.[89] This is confirmed by the decrease in the relative intensity of the D-band upon calcination of the commercial $CeO_2$ support. However, this effect could also be related to the decrease in SSA during calcination. Finally, the Raman spectra of the rod-based samples additionally contain a broad band between 250 and 300 cm$^{-1}$, which was formerly associated with the second-order transverse acoustic (2TA) mode but was recently assigned to the longitudinal stretch of the topmost Ce−O bond in a clean (111) surface.[90] Overall, the identified structural characteristics, i.e., surface defects and oxygen vacancies, of the different $CeO_2$ morphologies align well with the findings reported by previous studies for similar systems.[14] These trends are often supported by theoretical calculations of the different $CeO_2$ facets, while the high redox response of the surface sites has been demonstrated by spectroscopic investigations during catalytic reactions.[91−93]

After the addition of the NMs, no pronounced variations were observed in the Raman spectra with respect to the characteristic $CeO_2$ bands, aside from a decrease in the peak broadening and a blue shift of the $F_{2g}$ peak (from 453 to 458 cm$^{-1}$) relative to the bare rod-based support. These could be related to a slight increase in the crystallite size during the calcination of the impregnated catalysts.[12] Raman spectroscopy is also a powerful tool[32] to investigate the metal−support interaction in Pd-[32] and Pt-containing[12] ceria-based catalysts. In fact, as can be seen from Figure 3b, the samples PdPt-MF1-com and PdPt-MF2-cub show a band at 650 cm$^{-1}$, which was previously assigned to PdO ($B_{1g}$ mode),[94] and was observed if PdO clusters/NPs are present on the ceria surface.[95] PdPt-MF1-cub shows a weak band in this region, which suggests an intermediate Pd dispersion between those exhibited in the PdPt-MF1-com/PdPt-MF2-cub and PdPt-MF1-rod samples. These findings agree well with the STEM-EDX characterization data reported in Figure 2.

According to the characterization results obtained for the MF1 series, Pt is mostly present as a highly oxidized and well-dispersed species (Figures 2 and 3) in these samples. To confirm this state and the strong NM−$CeO_2$ interaction in the fresh catalysts, reference monometallic samples (Pt-IWI-com and Pd-IWI-com) were used for comparison. These samples

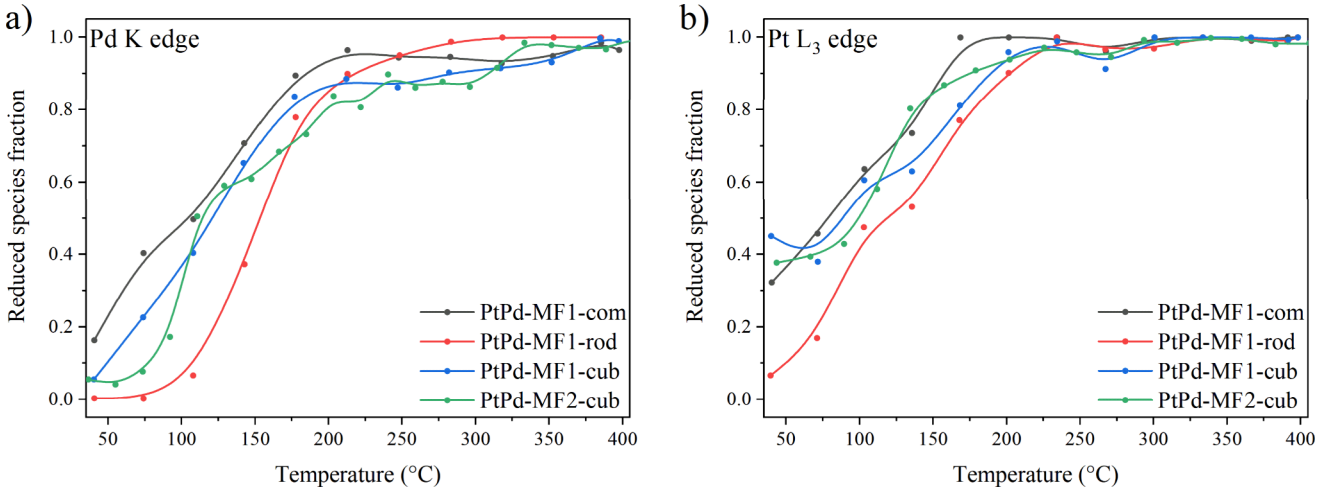


**Figure 4.** Results from LCA of the XANES region at (a) the Pd K edge and (b) the Pt $L_3$ edge during $H_2$-TPR (5%$H_2$/He, 10 °C/min) for the fresh bimetallic catalysts. Corresponding *R*-factors are reported in Figure S12a,b.



https://doi.org/10.1021/acs.jpcc.5c04366
J. Phys. Chem. C XXXX, XXX, XXX−XXX

were prepared by conventional incipient wetness impregnation followed by calcination in static air at 500 °C. Considering the low NM loading (SNMC below the monolayer[62]), this synthesis procedure is expected to lead to the formation of highly dispersed NM species, as widely reported in literature for such catalysts.[12,36,56,57,96] Several Pt species seem to be present in the Pt-IWI-com reference sample according to the corresponding Raman bands. On the one hand, the bands at 567 and 665 $cm^{-1}$ indicate the formation of $PtO_x$ species on the ceria surface.[12,97] These bands are also visible for PdPt-MF1-rod and, even if less pronounced, are distinguishable for PdPt-MF1-cub and PdPt-MF1-com. These structural characteristics indicate a similar interaction between $CeO_2$ and Pt for the MF1 series as that observed for the monometallic Pt-IWI-com reference sample. The appearance of minor bands at 550 and 690 $cm^{-1}$ suggests an even stronger Pt-ceria interaction for Pt-IWI-com, PdPt-MF1-rod, and PdPt-MF1-cub catalysts. However, the feature around 550 $cm^{-1}$ is superimposed by the characteristic D-band of nanocrystalline $CeO_2$ and is thus difficult to assign. In fact, both were associated with Pt-$CeO_2$ surface species containing a Pt−O−Ce linkage after calcination at 500 °C.[98] Only the band around 567 $cm^{-1}$ is discerned for the PdPt-MF2-cub catalyst, indicating the presence of a $PtO_x$ species. For this sample, the small shoulder noticed around 550 $cm^{-1}$ suggests a weaker interaction of Pt with the ceria support.

The *ex situ* XANES measurements at the Pt $L_3$ and Pd K edges (Figure S11) revealed that both NMs are in highly oxidized states in all fresh bimetallic samples. This state is expected due to the high dispersion of the NM species and the catalyst exposure to the ambient atmosphere after synthesis. The corresponding FT-EXAFS spectra at the Pd K edge (Figure S23) with their less pronounced second coordination shell, confirm the high dispersion of Pd and Pt on the ceria surface.

**3.2. Dynamics in the Noble Metal State Investigated by XAS during $H_2$-TPR.** To assess the redox behavior of the two NMs and further characterize their states in the fresh samples, *in situ* XAS measurements at Pd K and Pt $L_3$ edges were conducted during $H_2$-TPR experiments. Figure 4 depicts the results of the LCA of the XANES regions. At first, it is worth noting the difference in the initial (at ca. 40 °C) oxidation state of Pd and Pt among the samples upon the addition of the $H_2$-reductive gas mixture. While Pd species are mostly oxidized in all samples (0−18% of reduced species), Pt is already partially reduced to a similar extent (35−45% of reduced species) in all samples, apart from PdPt-MF1-rod, where the reduced Pt species account for only 5−10%. The same catalyst also shows the highest oxidation degree for Pd at room temperature, hinting once again at stronger metal−support interactions compared to the catalysts based on the other ceria morphologies. Despite the electron microscopy data indicating a different distribution and dispersion of Pd and Pt in the PdPt-MF1-cub and PdPt-MF2-cub catalysts, very similar starting oxidation states were identified for both NMs in these samples.

From the LCA of the Pd K edge XANES spectra, some differences in the reducibility of Pd species were observed among the MF1 catalysts. The reduction of Pd starts around 80 °C in the PdPt-MF1-rod catalyst, while for the samples supported on commercial ceria and nanocubes, the formation of metallic Pd begins already at 40 °C. In accordance with the ranking of the reduction onset, increasing values of $T_{50,\,red}$ (temperature of 50% reduction of $Pd^{2+}$ species) were found for $CeO_2$-com, -cub, and -rod samples, namely 109, 121, and 154 °C. The PdPt-MF1-cub and PdPt-MF1-com catalysts show a rather similar Pd reduction profile, with two reduction zones up to 210 °C and up to 400 °C, which most probably correspond to different Pd species. Pd stabilized by the ceria lattice as single atoms was reported to be less reactive compared to Pd NPs.[37,99] Moreover, Hu *et al.*[31] showed that Pd on ceria nanorods is linked via $Pd^{2+}$−$O^{2-}$−$Ce^{4+}$ bonds to the surface, which are expected to be more resistant toward reduction. In comparison, a sharper NM reduction profile was observed for the PdPt-MF1-rod catalyst around 150 °C, which could indicate a more uniform distribution of Pd species. These trends are in line with the characterization data reported above, indicating the formation of PdO-like entities and also of highly dispersed species having a strong interaction with the $CeO_2$-com and -cub supports, whereas only the latter NM state was recognized for the PdPt-MF1-rod catalyst. Herein, despite the same batch of PdPt bimetallic particles was used for the preparation of all the catalysts, the effect of the support morphology and porosity on the structure of the NPs in the as-prepared catalysts is recognizable.

While at the onset of the $H_2$-TPR experiment, the fraction of reduced Pt was around 40% in the MF1-cub, MF2-cub, and MF1-rod samples, the temperature at which 70% of the Pt species are reduced ($T_{70,red}$) was used as a second indicator to compare the reducibility of the bimetallic catalysts. The following values were obtained for the PdPt-MF1-com, PdPt-MF1-cub, and PdPt-MF1-rod samples, respectively: 124, 148, and 160 °C (Figure 4b). Despite the small differences in $T_{70,red}$, similar reduction profiles were observed for the samples of the MF1 series. Complete Pt reduction was more easily achieved on the commercial ceria support (around 170 °C), whereas temperatures of 220−230 °C were necessary for the full reduction of Pt in the PdPt-MF1-cub and PdPt-MF1-rod samples. Interestingly, for the sample containing alloyed PdPt particles (PdPt-MF2-cub), a steep and significant Pt reduction was measured around 120 °C, while the NM reduction profile above 200 °C matches that recorded for the corresponding PdPt-MF1-cub sample. Furthermore, the same trend was observed at around 100 °C for Pd, accompanied by the complete NM reduction only around 325 °C, which resembles the redox behavior of the analogous PdPt-MF1-cub sample.

In addition to the elucidation of the NM redox response through element-selective XAS investigations, the overall reducibility of the $CeO_2$ supports and supported bimetallic catalysts was assessed by thermogravimetric measurements (Figures S13 and S14). Considering that all catalysts were thermally treated in 10 vol % $O_2$/Ar up to 500 °C prior to the $H_2$-TPR experiment, the recorded mass loss is solely due to the reduction of the NM oxides and $CeO_2$ and not because of $H_2O$ and $CO_2$ desorption. In contrast to the reduction profiles of the pure $CeO_2$ supports showing only a slight reduction below 500 °C (Figure S13), two temperature regions can be distinguished in the TG signal recorded for the bimetallic Pd−Pt catalysts: a more pronounced mass loss up to ca. 200 °C and a steady mass loss up to 500 °C. As illustrated by the *in situ* XAS measurements reported in Figure 4 and the water evolution displayed in Figure S14), the reduction of Pd and Pt contributes especially up to 200 °C to the recorded mass loss, whereas at higher temperatures, the major contribution originates from the support reduction. However, considering that the reduction of the NM is followed immediately by the reduction of the $CeO_2$ surface[100] due to the $H_2$ spillover, a


https://doi.org/10.1021/acs.jpcc.5c04366
J. Phys. Chem. C XXXX, XXX, XXX−XXX

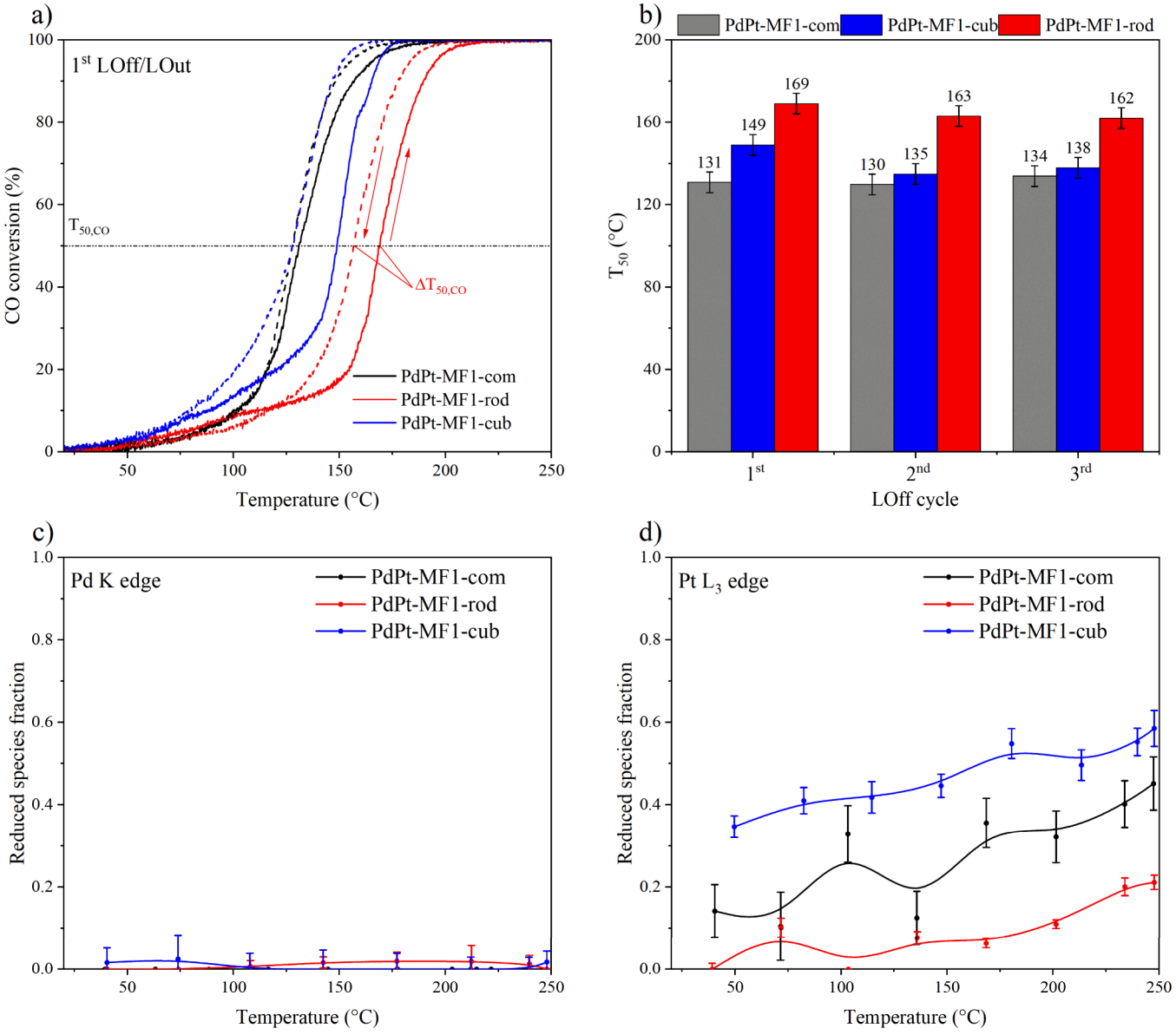


**Figure 5.** (a) 1st LOff (full lines) and LOut (dotted lines) CO conversion curves and (b) $T_{50,CO}$ measured for the fresh PdPt bimetallic catalysts of the series MF1 based on $CeO_2$ supports with three different morphologies. Relative fraction of reduced species as obtained by LCA of the *operando* XANES data collected at the (c) Pd K edge and (d) Pt $L_3$ edge during the 1st CO oxidation LOff for the fresh catalysts. Corresponding *R*-factors are reported in Figure S12c,d.

clear separation of the two processes is difficult. Overall, although the reduction below 200 °C is less affected by the sample characteristics, the total mass loss up to 500 °C aligns well with the SSA of the different supports. This tendency is caused by the location of most of the oxygen vacancies on the $CeO_2$ surface.[1]

**3.3. Influence of the $CeO_2$ Support on the Catalytic Activity.** In the next step, the impact of the $CeO_2$ morphology and the resulting interaction with Pd and Pt were systematically evaluated during CO oxidation. CO conversion was determined in a model gas mixture containing 1000 ppm of CO and 10 vol % $O_2$ in He during three consecutive light-off/light-out (LOff/LOut) cycles between 25 and 300 °C. This procedure was selected to mimic the transient conditions present in the exhaust of lean combustion engines. The total NM amount in the reactor was kept constant for all the samples of the MF1 series by adjusting the catalyst weight loaded in the capillary. This procedure allowed us to monitor the variations in activity that likely appear due to fast structural changes under reaction conditions, and to compare the performance of the different samples once the system has reached a steady state. Figure 5a depicts the first LOff/LOut cycle for the catalysts of the MF1 series. The complete cycles for all fresh bimetallic catalysts and the monometallic reference samples are reported in Figures S15 and S16a,b. Despite their similar SNMC, the samples showed different catalytic performances, as reflected by the $T_{50,CO}$ (temperature of 50% CO conversion, Figure 5b) values and the profiles of the low temperature activity (below 100 °C, Figure 5a). For the fresh catalyst state, the best CO oxidation performance was shown by PdPt-MF1-com ($T_{50,CO}$ = 131 °C), followed by the PdPt-MF1-cub ($T_{50,CO}$ = 149 °C) sample. In contrast, a significantly lower activity was displayed by the PdPt-MF1-rod catalyst, which converts 50% CO only at 169 °C. These activity


https://doi.org/10.1021/acs.jpcc.5c04366
J. Phys. Chem. C XXXX, XXX, XXX−XXX

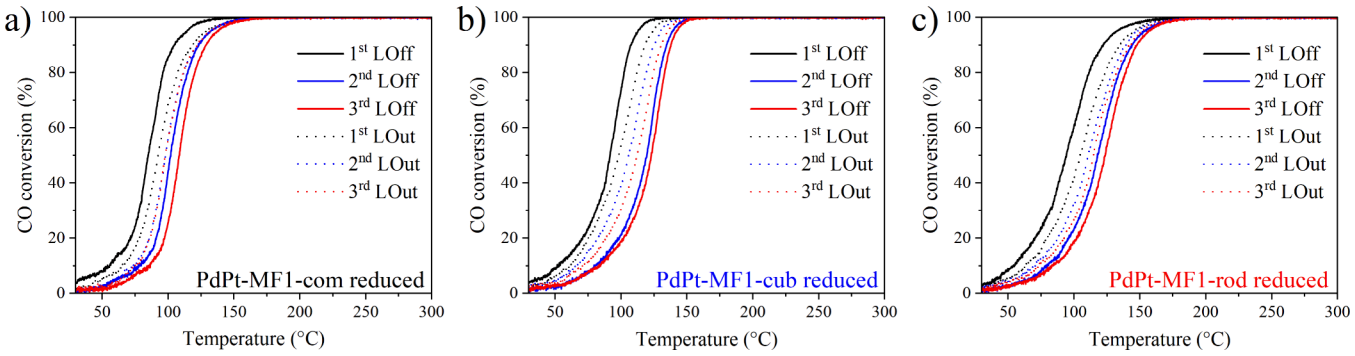


**Figure 6.** CO conversion during 3 consecutive LOff/LOut cycles measured for the 3 PdPt bimetallic catalysts of the -MF1 series after mild reduction. (a) PdPt-MF1-com; (b) PdPt-MF1-cub; and (c) PdPt-MF1-rod.

trends could be explained by different metal−support interactions, with the PdPt-MF1-rod catalyst containing exclusively highly dispersed species, which are less active for oxidation reactions.[37,62,101] The obtained CO conversion profiles of the fresh bimetallic PdPt-MF1 samples align with those shown by the Pt monometallic catalyst (Figure S16b). Only small variations were noticed within the applied temperature range for the PdPt-MF1-cub and PdPt-MF1-com samples, while a slightly lower activity was measured for the PdPt-MF1-rod catalyst. A normal hysteresis profile was identified for all samples, with a more defined loop for PdPt-MF1-rod and PdPt-MF1-cub. Such a difference in activity during the LOut vs LOff CO oxidation curves has been associated with different effects, including NM particle size, NM−CO interaction, NM oxidation/reduction, but also with mass and heat diffusion effects.[102,103] For monometallic Pt/$Al_2O_3$ catalysts, a normal hysteresis was found to occur during CO oxidation if the NM particle size is above ∼2 nm.[17] For Pd/$CeO_2$-based catalysts, not only structural dynamics induced by CO but also the interaction with $CeO_2$ leading to NM clustering/redispersion affect the hysteresis profile.[24] A pronounced hysteresis in the activity profile was also reported for PdPt/$Al_2O_3$ bimetallic catalysts during $CH_4$ oxidation, which was related to the kinetics of Pd reduction/reoxidation in Pd segregated domains on the alloyed particle surface.[104] In contrast, on a $CeO_2$−$ZrO_2$ support, the NM redox dynamics are promoted, and a narrow hysteresis was observed.[105]

In our study, in addition to the hysteresis profile, a small improvement in catalytic activity was noticed for PdPt-MF1-cub and PdPt-MF1-rod catalysts after the first LOff/LOut cycle, with a $\Delta T_{50,CO}$ between the first and the second LOff of 14 °C and 6 °C toward lower temperatures, respectively. Hence, during the transient measurements, the observed changes in catalytic activity most probably encompass also more permanent structural changes, as it is shown in the following. In particular, the detected activity improvement strongly resembles the behavior of the Pt-IWI-com sample (Figure S16b), which shows a $\Delta T_{50,CO}$ between the first and the second LOff of ∼−20 °C. On the other hand, the PdPt-MF1-com sample that already contains small Pd and Pt clusters (Figures 2a−c and S8) does not exhibit this behavior during the CO oxidation cycles (Figure 5b). For all samples, no significant variations in activity were observed between the second and third cycles (Figure 5b), which indicates stabilization of the catalyst structure. The complete LOff/LOut cycles measured for the 3 fresh PdPt-MF1 catalysts are reported in Figure S15.

The overall CO oxidation activity trend of PdPt/$CeO_2$-commercial > PdPt/$CeO_2$-cubes > PdPt/$CeO_2$-rods that was obtained in this study cannot be directly compared with previous literature data. To the best of our knowledge, this is the first study of bimetallic PdPt catalysts supported on different $CeO_2$ morphologies. However, while the investigations on monometallic Pt/$CeO_2$ and Pd/$CeO_2$ catalysts suggest that $CeO_2$ rods promote the low temperature conversion of CO,[30,106] our results identified the $CeO_2$-cubes as a more suitable morphology for CO oxidation catalysts. Besides the slightly different reaction conditions, the SNMC and the dynamic structural changes of Pt and Pd are often disregarded when evaluating such systems, which leads to distinct activity profiles encompassing multiple structural effects.

For such highly dispersed Pt/$CeO_2$-based catalysts, the formation of slightly reduced Pt species under reaction conditions was found to be necessary for the onset of CO oxidation during the LOff/LOut cycles.[36,62] Starting with Pt/Pd single sites or highly dispersed species in $CeO_2$-supported monometallic catalysts, the migration and formation of multinuclear entities/clusters was uncovered by previous *in situ/operando* studies.[24,62] Particularly, at low temperatures the reductive effect of CO is expected to affect the NM state, while at high temperatures and complete CO conversion NM reoxidation/redispersion on $CeO_2$ is predictable.[13,17,21,100,107] Hence, the increased activity of the bimetallic Pd−Pt catalysts after the first LOff could be due to the partial reduction and formation of slightly larger NM clusters.

In order to verify this hypothesis and study the behavior of the two NMs under the reaction conditions, *operando* XAS measurements were conducted at Pd K and Pt $L_3$ edges during the first LOff cycle. The results of the LCA of the XANES regions are displayed in Figure 5c,d for Pd and Pt, respectively. For all MF1 catalysts, partial reduction of Pt was observed while ramping up in the reaction mixture to 250 °C, with higher reduction degrees (40% and 55%) observed for the MF1-com and MF1-cub supported samples, respectively. At the same time, Pd remained in an oxidized state, with no noticeable change in the local structure in all catalysts. In this regard, small $PdO_x$ clusters generated *in situ* under similar reaction conditions were shown to be the active species for CO conversion at low temperatures.[37] The reoxidation of Pt species was not observed for the bimetallic Pd−Pt samples even at complete CO conversion, which suggests that either the reduced Pt could be stabilized in the presence of Pd or some unconverted CO could still be present at the probed spot


https://doi.org/10.1021/acs.jpcc.5c04366
J. Phys. Chem. C XXXX, XXX, XXX−XXX

(middle of the catalyst bed).[21,107] Overall, the observed structural changes led to the promotion of the CO oxidation activity over the PdPt-MF1-com and PdPt-MF1-cub samples. This improvement in activity is already observed during the first reaction LOut (dotted lines in Figure 5a), which shows a normal hysteresis profile that is typically observed for larger (>2 nm) Pt particles.[17] The activity and LOff/LOut loops are maintained during the following cycles, indicating catalyst stabilization (Figure S15). Despite the investigation of Ce state under reaction conditions would be as well highly relevant for further understanding the catalyst structural evolution and the CO oxidation mechanism, such *operando* XAS measurements would require a more elaborate approach and the adjustment in sample composition due to the highly absorbing ceria support,[37,100] and should be investigated in a future study.

In the next step, the influence of a mild reductive treatment on the catalyst activity was investigated for the Pd−Pt/$CeO_2$ samples supported on different ceria morphologies. After reduction in 5 vol % $H_2$/He at 300 °C for 30 min, 3 CO oxidation LOff/LOut cycles were conducted in the same temperature range (Figure 6). The LCA of the XANES data obtained during the $H_2$-TPR experiment (Figure 4) shows almost complete reduction of Pd and Pt below 300 °C. A pronounced improvement in the CO oxidation activity is observed for all reduced catalysts, with a drop in the $T_{50,CO}$ between the third and fourth LOffs of up to 68 °C for the PdPt-MF1-rod catalyst. An even more pronounced activation after reduction was measured for the corresponding monometallic Pt-IWI-com and Pd-IWI-com reference catalysts, with a drop in the $T_{50,\,CO}$ of 86 and 89 °C, respectively. 50% CO conversion is achieved over these two catalysts already at 40 and 44 °C, respectively.

This enhancement of the CO oxidation activity for the reduced monometallic catalysts points out a detrimental effect of Pd−Pt copresence/alloying for the activity of $CeO_2$-based catalysts. A direct comparison of the observed activity trends with previous literature is not simple due to the lack of analogous studies combined with a high degree of heterogeneity of most investigated bimetallic catalysts, i.e., alloying extent, nanoparticle size distribution, and different SNMC. In general, bimetallic Pd−Pd catalysts supported on alumina were reported to show either a higher or a lower activity relative to that measured for monometallic Pt- or Pd-only systems, depending on the CO concentration, gas mixture, Pd−Pt loading/ratio, and interaction, as well as on the nanoparticle surface composition.[108−110] On strongly interacting supports such as $CeO_2$, the interaction with the two noble metals, and the resulting perimeter sites[25] or the variation in the number of NM active sites that are *in situ* generated,[16] could also contribute to the observed activity trends. In addition, for all the reduced bimetallic catalysts of the MF1 series and especially for the reduced monometallic references, a steady increase in $T_{50,\,CO}$ values was observed over consecutive LOff/LOut cycles (4th to 6th cycle, Figure S17), which suggests the low stability of the reduced species and their possible redispersion under reaction conditions. The increase in $T_{50,\,CO}$ between the fourth and sixth LOffs for the monometallic Pd-IWI-com and Pt-IWI-com samples is quite significant, respectively amounting to 65 and 57 °C. In contrast, for the 4 bimetallic catalysts, the corresponding increase in $T_{50,\,CO}$ is lower (between 25 and 35 °C), suggesting a higher structural stability.

TEM investigations of the spent MF1 samples (catalyst after prereduction and 3 LOff/LOut CO oxidation cycles, thus after the sixth cycle) revealed the presence/copresence of different NM entities in the investigated samples (Figure 7). Additional

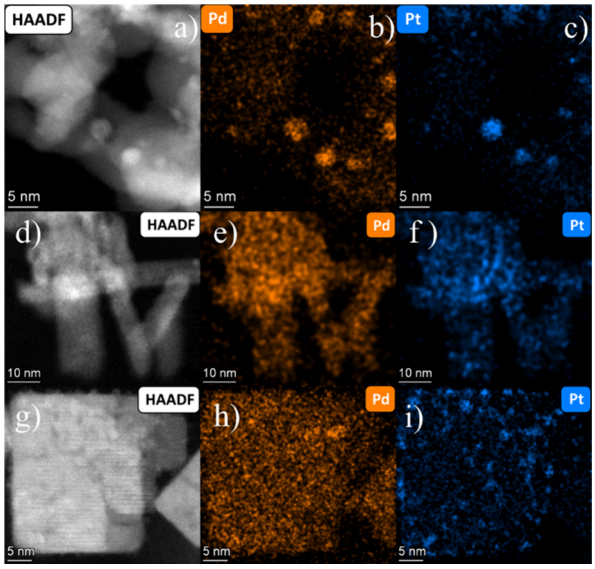


**Figure 7.** HAADF-STEM images of the spent PdPt bimetallic catalysts, namely, PdPt-MF1-com (a), PdPt-MF1-rod (d), and PdPt-MF1-cub (g). EDXS elemental mapping for Pd (b, e, h) and Pt (c, d, i) corresponding to the HAADF-STEM images.

images of the spent catalysts are available in the Supporting Information in Figures S26 and S27. Whereas highly dispersed NM species (single atoms/clusters) were observed in all samples, for the PdPt-MF1-com catalyst, heterogeneously intermixed Pd−Pt NPs (3−4 nm) are also identified (Figure 7a−c). Small bimetallic subnanometer Pd−Pt clusters and pure Pt NPs (1−2 nm) seem to be formed in the PdPt-MF1-cub catalyst, but they are hardly visible in the PdPt-MF1-rod sample. The formation of monometallic or alloyed Pd−Pt particles is likely induced during the $H_2$-prereduction step. Considering that all samples were treated in the same manner for a relatively long time (30 min at 300 °C), an identical SNMC was applied, and at 300 °C Pd and Pt are mostly in a reduced state in all catalysts (Figure 4), the migration of the formed metallic entities and the generation of larger monometallic/alloyed NPs are theoretically occurring with a similar probability in all samples since the interaction with the support surface has diminished. This assumption is supported by the comparable behavior of the noble metals during the transient $H_2$-TPR experiments (Figure 4), despite their different interaction with the ceria supports under oxygen-rich conditions, i.e., via NM−O−Ce bonds.[37,62,100] Therefore, the observed differences in the NM state after prereduction and 3 LOff/LOut cycles are most probably due to the *in situ* oxidation/redispersion of the formed NPs at high temperatures when the CO conversion is completed.[21] This process seems to be affected by the $CeO_2$ morphology. In this regard, the different number of oxygen vacancies present in the used $CeO_2$ supports (Table 2) is most probably the root of the more or less pronounced NM redispersion. It is well-known that $CeO_2$-rods contain a high number of defect sites,[83] which are expected to impact the Pd[30] and Pt redispersion process under reaction conditions. However, the influence of the ceria


https://doi.org/10.1021/acs.jpcc.5c04366
J. Phys. Chem. C XXXX, XXX, XXX−XXX

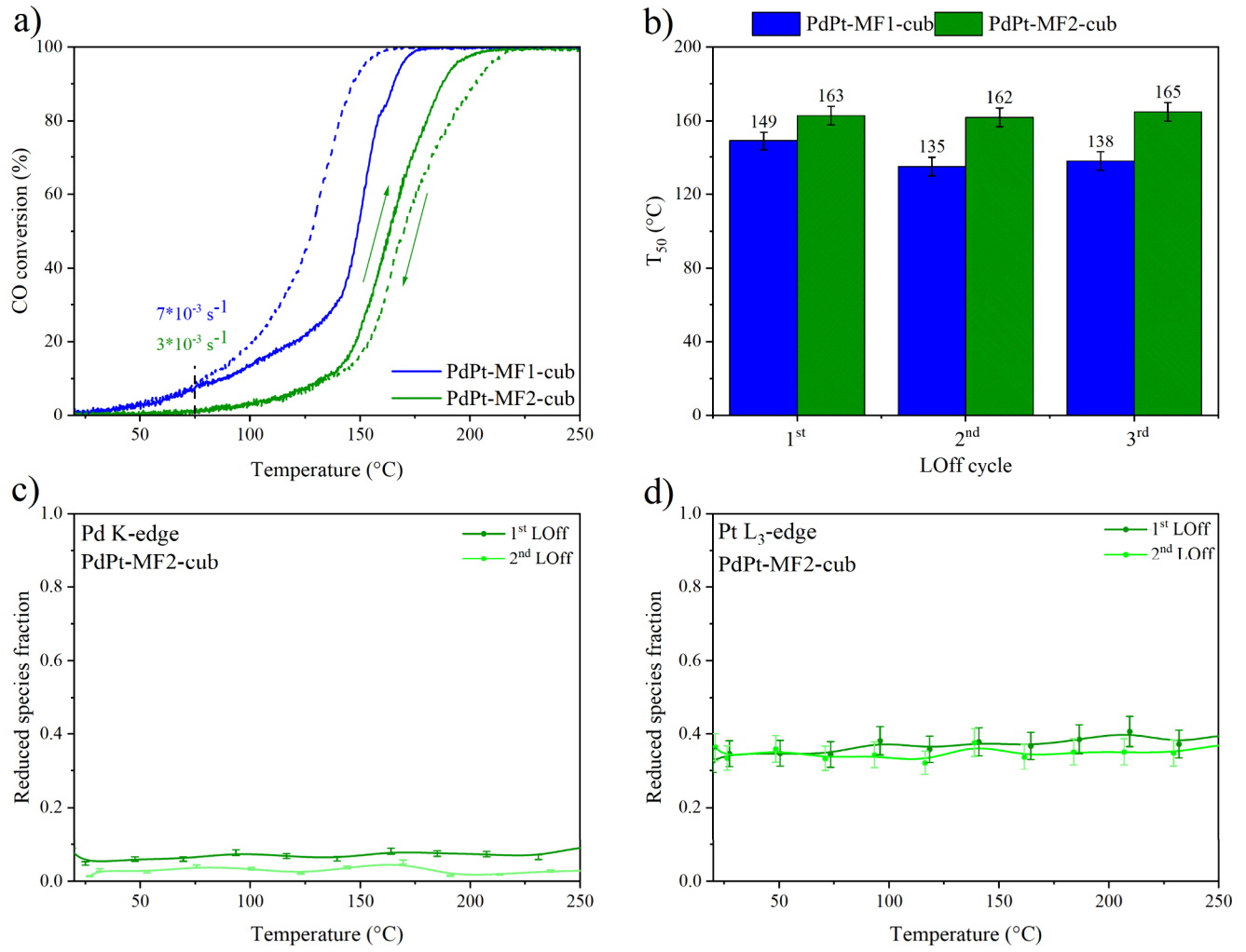


**Figure 8.** (a) 1st LOff (full lines) and LOut (dotted lines) CO conversion curves and (b) $T_{50,CO}$ measured for the PdPt bimetallic fresh catalysts with different Pd−Pt initial interaction degree supported on $CeO_2$ nanocubes. Blue curves/bars: dispersed Pd and Pt entities. Green curves/bars: alloyed PdPt NPs. Relative fraction of reduced species as obtained by LCA of the *operando* XANES data collected at the (c) Pd K edge and (d) Pt $L_3$ edge during two consecutive CO oxidation LOffs for the fresh PdPt-MF2-cub catalyst. Corresponding *R*-factors are reported in Figure S12e,f.

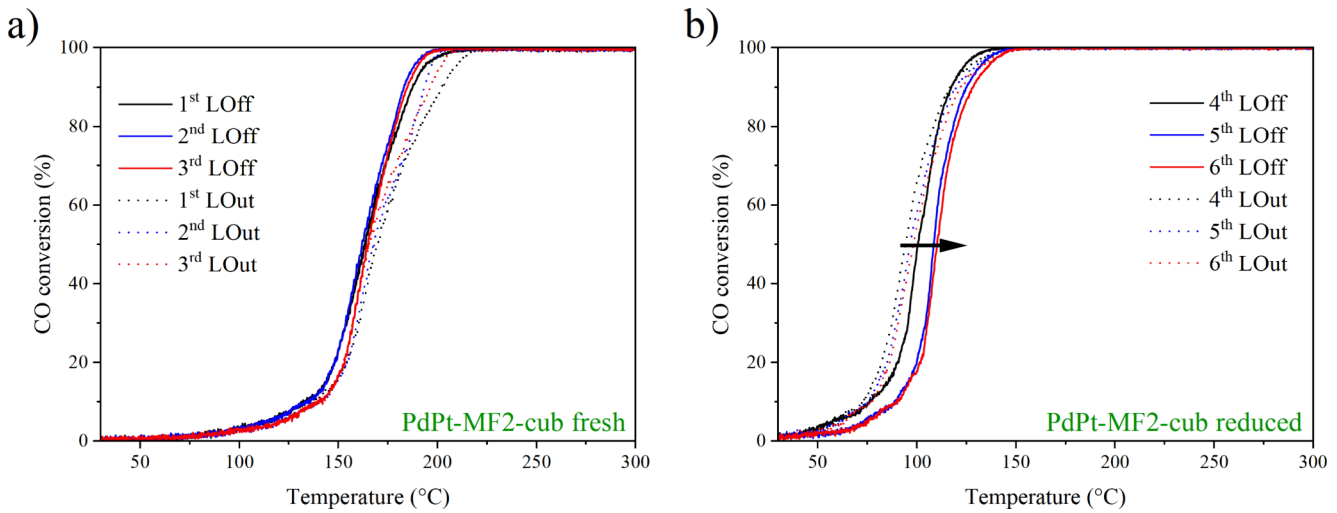


**Figure 9.** CO conversion during consecutive LOff/LOut cycles measured for the PdPt-MF2-cub sample (a) in the fresh state and (b) after mild reduction.

structural peculiarities on the NM migration and alloying already during the prereduction step cannot be completely ruled out. Herein, the reduced number of oxygen vacancies of the commercial ceria support due to the high temperature



https://doi.org/10.1021/acs.jpcc.5c04366
J. Phys. Chem. C XXXX, XXX, XXX−XXX

calcination clearly promotes the formation of Pt- and Pd-rich agglomerates during catalyst preparation (Figures 2a–c and S8) and most probably endorses the formation of alloyed particles during $H_2$-reduction. The ceria nanocubes show an intermediate interaction with Pt, as evidenced by facile reduction under the reaction conditions (Figure 5d). This is in line with the STEM-EDX results on the spent PdPt-MF1-cub catalyst, which show a higher dispersion of Pd compared to that of Pt in this sample (Figure 7g–i).

**3.4. Influence of the Initial Pd–Pt Interaction on the Catalytic Activity and Structural Evolution.** In order to evaluate the impact of a stronger Pd–Pt interaction on the structural dynamics of Pd–Pt/$CeO_2$ catalysts, a direct comparison of the behavior of PdPt-MF1-cub and PdPt-MF2-cub samples was done in the next step. Through a more facile reduction of $Pt^{4+}$, as described in the experimental section, the coreduction of Pd and Pt was promoted during the microfluidic synthesis. This protocol led to the formation of alloyed Pd–Pt particles (MF2), which were subsequently deposited on $CeO_2$-nanocubes (Figure 2j–l).

Clear differences in the catalytic performance were noticed during the CO oxidation LOff/LOut cycles conducted for the fresh samples. A higher $T_{50,CO}$ temperature was measured for the fresh PdPt-MF2-cub catalyst than for the analogous fresh sample containing highly dispersed NM species (PdPt-MF1-cub). The calculation of the turnover frequency (TOF) at 75 °C, based on the mean particle size of 2.8 nm for the PdPt-MF2-cub catalyst and the involvement of all metal sites in PdPt-MF1-cub, resulted in an almost double value for the latter sample (0.0030 vs 0.0072 $s^{-1}$, respectively). These results suggest that the presence of alloyed Pd–Pt particles on the surface of $CeO_2$-nanocubes does not represent a benefit for CO oxidation, in comparison to the catalytic performance of the corresponding samples containing Pd and Pt monometallic species. Additionally, an inverse hysteresis profile (i.e., lower activity during the LOut of CO oxidation LOut) was observed for the PdPt-MF2-cub catalyst during the first LOff/LOut cycle (Figure 8a), which is in contrast to that observed for PdPt-MF1-cub. The same trend is maintained during the following LOff/LOut cycles (Figures 8b and 9a). Moreover, while a slight decrease of the $T_{50,CO}$ was noticed for PdPt-MF1-cub after the first LOff (Figure 8b), the activity of the PdPt-MF2-cub sample did not vary over consecutive LOff/LOut cycles. Analogous to the PdPt-MF1-com catalyst, this behavior suggests a higher structural stability of the larger and alloyed Pd–Pt NPs under reaction conditions.

Indeed, the *operando* XAS measurements conducted for the fresh PdPt-MF2-cub reveal rather stable and partially reduced Pt species during two consecutive LOff cycles (about 35–40% of Pt in the metallic state, Figure 8d). Similarly as it was observed for the previous set of samples (MF1), Pd remains mostly oxidized during CO oxidation.

After reduction in 5 vol % $H_2$/Ar at 300 °C for 30 min, both catalysts show improved activity compared to the fresh ones (Figure S16b–d), with a $T_{50,CO}$ of 92 and 101 °C for PdPt-MF1-cub and PdPt-MF2-cub, respectively. Nevertheless, while an inverse hysteresis was observed for all reduced catalysts of the MF1 series, a normal hysteresis profile (i.e., higher activity during the LOut) was recorded for the PdPt-MF2-cub sample (Figure 9b). Furthermore, even if both samples experienced an activity drop between the fourth and sixth LOff/LOut cycles, the extent of deactivation $\Delta T_{50,CO}$ is smaller for the sample containing prealloyed Pd–Pt clusters/NPs in comparison to PdPt-MF1-cub. Thus, a $\Delta T_{50,CO}$ of only +10 °C was measured for the PdPt-MF2-cub sample versus ∼+30 °C observed for the PdPt-MF1-cub catalyst. As previously discussed, the reason for this deactivation behavior might be the reoxidation and redispersion of the NM particles due to the interaction with ceria at higher temperatures, with complete CO conversion.

To verify this hypothesis, the oxidation state of both Pd and Pt was monitored for the prealloyed (PdPt-MF2-cub) and prereduced catalyst by *operando* XAS during CO oxidation LOff in reaction mixture. The results of the LCA for the Pt $L_3$ and Pd K edge *operando* XANES data are shown in Figure 10.

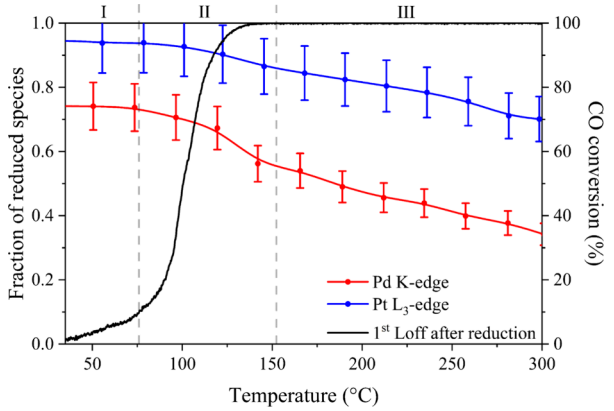


**Figure 10.** Relative fraction of reduced species (left *y* axis) as obtained by LCA of the *operando* XANES spectra collected at the Pd K edge (red line) and the Pt $L_3$ edge (blue line) during CO oxidation LOff after $H_2$-TPR to 300 °C for the PdPt-MF2-cub catalyst. CO conversion (black line) measured during the *operando* experiment can be read on the right *y* axis. Region I shows a stable Pd/Pt oxidation state; region II shows pronounced oxidation of Pd and Pt; region III displays a continuous oxidation of Pd and Pt. Corresponding *R*-factors are reported in Figure S12g,h.

During ramping up in the reaction mixture, Pd appears more susceptible to reoxidation under lean conditions, with the $Pd^0$ fraction dropping from 75% to 35%. The fraction of reduced Pt species, instead, drops only from 95% to 70%. For both NMs, the change in oxidation state follows the course of CO depletion.

To confirm the nature and the evolution of the Pt and Pd species in the different bimetallic samples, *in situ* DRIFTS measurements were conducted for the fresh and prereduced catalysts before and after a LOff/LOut cycle between 30 and 300 °C in 1000 ppm of CO, 10 vol % $O_2$/Ar. The obtained results are reported in Figure 11. In line with previous literature findings[37,111,112] for $CeO_2$-supported catalysts, the analysis of the deconvoluted *in situ* DRIFTS spectra for the fresh Pt or Pd monometallic references confirmed the high dispersion of the noble metal species. This outcome aligns well with the XRD and Raman characterization data (Figure 3). For the Pt-IWI-com reference, three main contributions were observed for the fresh catalyst before the CO oxidation LOff (Figures 11a and S17a): at 2115, 2098, and 2084 $cm^{-1}$, which were previously assigned to CO linearly adsorbed on isolated Pt atoms ($Pt_{iso}$),[112] CO on ionic $Pt^{2+}$ at the NM–$CeO_2$ interface[93] and on $Pt^0$ terrace-like sites,[113] respectively. The IR bands appearing at lower wavenumbers were attributed to CO linearly adsorbed on low-coordinated Pt atoms (e.g., steps and edge sites) that are typically present on subnanometer Pt NPs. No contribution was observed between 2000 and 1800


https://doi.org/10.1021/acs.jpcc.5c04366
J. Phys. Chem. C XXXX, XXX, XXX–XXX

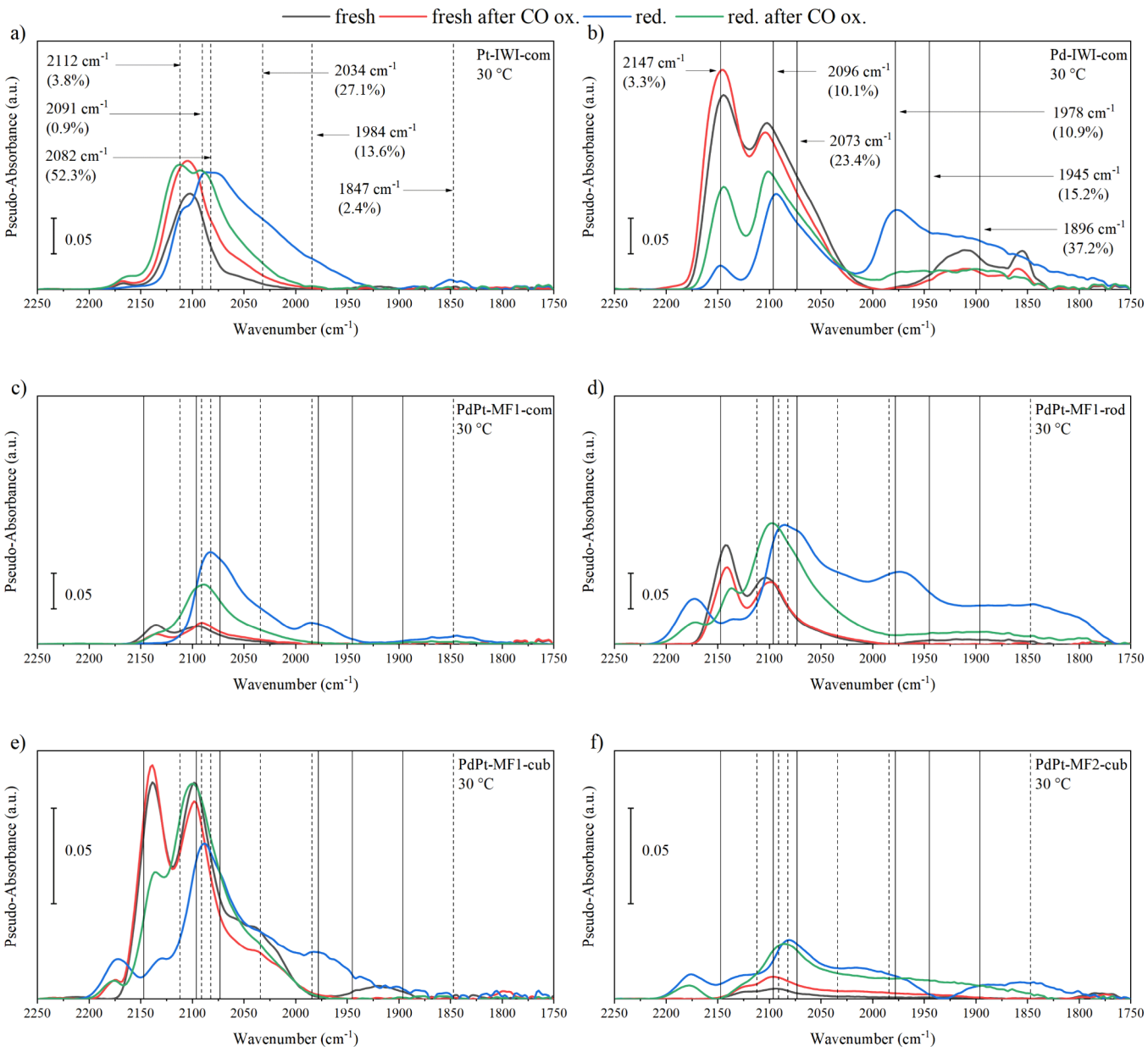


**Figure 11.** *In situ* DRIFTS spectra obtained for all investigated catalysts at 30 °C in 1000 ppm of CO, 10 vol % $O_2$, and Ar balance after background subtraction. Black spectra were collected for the fresh state, red spectra after a LOff/LOut cycle. Blue spectra were collected for the reduced catalyst state, green spectra after a LOff/LOut cycle. Background features centered around 1600 $cm^{-1}$ are related to water vapor. Solid and dotted vertical lines correspond to the Gaussian peaks obtained by deconvolution fit of the spectra collected for the Pt and Pd monometallic reference catalysts after prereduction, respectively. The values in parentheses represent the relative area (%) below the peaks obtained from the fit.

$cm^{-1}$, a region previously linked to bridged CO on metallic Pt.[93] This is in agreement with the absence of larger NM nanoparticles in this sample (XRD data are given in Figure 3a). The small band around 2167 $cm^{-1}$ could be caused by the CO in the gas phase or due to the CO adsorption at $Ce^{3+}$ defect sites.[62,112,114] After the LOff/LOut cycle (Figure S17b), an increase in the intensity of all bands was observed, combined with the disappearance of the contribution at 2098 $cm^{-1}$. Additionally, a slight red shift was noticed while the remaining IR band components of the deconvoluted spectra are now centered at 2107 and 2073 $cm^{-1}$. This trend indicates a slight reduction of Pt in the reaction mixture, as reported also in previous studies.[17,62] After catalyst reduction (Figure S17c) in 5 vol % $H_2$/Ar at 300 °C, a rather broad band was noticed below 2090 $cm^{-1}$. In general, the literature assigns this region to CO bonded to reduced/partially reduced Pt.[36,61,93,112,115,116] For instance, Resasco *et al.*[116] ascribed for a $Pt/CeO_2$ catalyst upon $H_2$-reduction up to 450 °C the appearance of a band around 2060 $cm^{-1}$ of CO adsorbed on reduced Pt clusters. The decrease of the bands around 2100 $cm^{-1}$ and the appearance of bands at lower wavenumbers, i.e., 2090 and 2065 $cm^{-1}$, was also reported by Gänzler *et al.* after reduction of a $CeO_2$-based catalyst at 250 °C. Also, for the Pt-IWI-com catalyst, two major contributors were identified after deconvolution of the *in situ* DRIFTS data due to the mild reduction conditions, which are centered at 2082 and 2034 $cm^{-1}$. In this regard, the residual of the high frequency peak at 2112 $cm^{-1}$ is still present, indicating that some isolated noble metal atoms are remaining. Lastly, a small, double peak around 1850 $cm^{-1}$ appears, which could be related to bridged CO on


https://doi.org/10.1021/acs.jpcc.5c04366
J. Phys. Chem. C XXXX, XXX, XXX−XXX

Pt clusters.[117] After the LOff/LOut cycle, the DRIFTS spectrum of the prereduced Pt-IWI-com catalyst resembles the one recorded for the fresh catalyst at the same reaction stage (Figures S17d vs b). Nonetheless, the contributions around 2115 and 2085 $cm^{-1}$ are better resolved, suggesting the redispersion of the noble metal under reaction conditions and the formation of partially oxidized Pt.

Also for the Pd-IWI-com reference catalyst, the assignments for the deconvoluted CO adsorption DRIFTS data (Figure S18) were done based on previous literature studies on similar systems.[22,37,61,111,112,118−122] Accordingly, the peak around 2143 $cm^{-1}$ (denoted as CO-$Pd_{iso}$) was attributed to linearly bound CO on highly dispersed and oxidized Pd atoms.[61,119−122] The contribution around 2106 $cm^{-1}$ (denoted as CO-Pd-$L_1$) was linked to CO linearly bound to partially reduced Pd atoms that are present in small Pd clusters.[37,61,122] Additional contributions to the IR bands above 2000 $cm^{-1}$ (denoted as CO-Pd-$L_2$) were assigned to CO linearly adsorbed on corners, edges, and steps of Pd clusters.[122] Lastly, the bands below 2000 $cm^{-1}$ were correlated to bridged carbonyls on metallic Pd species[37,112,120,122] as well as to bridged CO adsorption on the $CeO_2$ surface or at the Pd-$CeO_2$ interface.[111] Notably, the band at ca. 1850 $cm^{-1}$ exhibited by the Pd-IWI-com sample before reduction was previously assigned to CO on 3-fold hollow Pd sites.[122] Overall, in the Pd-monometallic reference sample, most NM species are highly dispersed and oxidized as isolated atoms or small Pd clusters, in line with the XRD data (Figure 3). No major structural change was identified after the LOff/LOut CO oxidation cycle (Figure 11b). Only a slight decrease in the intensity of the IR bands appearing below 2000 $cm^{-1}$ was noticed, together with a decrease of the bands present at lower wavenumbers. On the contrary, after the reductive treatment, the IR fingerprints of bridge carbonyls are clearly visible below 2000 $cm^{-1}$, confirming the formation of reduced Pd clusters/NPs (Figure S18c). The deconvolution of the DRIFTS spectrum uncovered three major contributors (ca. 63% of the area below the curve) at around 1978, 1944, and 1895 $cm^{-1}$. Due to the reoxidation and partial redispersion of Pd during the following LOff/LOut cycle, this composite band strongly decreases its intensity in favor of the bands previously assigned to more oxidized and/or dispersed Pd species (Figure S18d). This dynamic change in the structure of prereduced Pd/$CeO_2$-based catalysts in oxidative atmospheres (lean conditions) has been previously reported in the literature for similar systems.[22]

The corresponding in situ DRIFTS spectra collected for the fresh and prereduced Pd−Pt bimetallic catalysts before and after the CO oxidation LOff/LOut cycle are reported in Figure 11c−f. Similarly to the case o Pt and Pd monometallic references, all spectra were deconvoluted using a Gaussian fitting function to identify the different contributions (Figures S19−S22). Based on previous investigations on CO adsorption on Pd−Pt bimetallic catalysts, slight variations in the band position are expected depending on the sample structure and experimental conditions. In this regard, Grill and Gonzales[123] reported a shift of about 10 $cm^{-1}$ of the CO adsorption bands toward higher frequencies for a Pd−Pt/$SiO_2$ catalyst in comparison to the corresponding monometallic catalyst. The authors assigned the CO adsorption band at 2095 $cm^{-1}$ to CO linearly adsorbed on Pd, the band at 2075 $cm^{-1}$ to linearly bound CO on Pt, and the bands below 2000 $cm^{-1}$ exclusively to bridged CO on Pd. More recently, Martin *et al.*[41] conducted an *in situ* DRIFTS study during transient CO oxidation over a series of Pd−Pt/$Al_2O_3$ catalysts and reported different trends depending on the Pd:Pt ratio and catalyst pretreatment. At high Pt concentrations, linearly adsorbed CO on metallic Pt was found to dominate the spectrum with a band between 2080−2090 $cm^{-1}$, while bridged-bonded and linearly bonded CO (2050−2070 $cm^{-1}$) are claimed to be formed at high Pd concentrations in the bimetallic catalysts. For similar Pd and Pt amounts, the authors reported broadening of the bands below 2000 $cm^{-1}$. The influence of the Pd:Pt ratio on the CO adsorption features of an alumina-supported catalyst was also investigated by Hazlett *et al.*[109] under lean reaction conditions. The study attributed the CO adsorption peak around 2090 $cm^{-1}$ to a single linear carbonyl formed on Pd or Pt, while the feature at 2111 $cm^{-1}$ was correlated to the formation of dicarbonyls (CO-NM-CO) if a second band around 2050 $cm^{-1}$ is present or linear carbonyl attached to Pt and atomic oxygen (CO-NM-O).

In our study, the DRIFTS spectra are dominated by two well-defined peaks between 2000−2175 $cm^{-1}$ (Figures S19−S22), a region previously assigned to CO adsorbed at ($Pt_{iso}$),[112] Pt(cluster)−$CeO_2$ interface,[93] and $Pt^0$ terrace-like sites[113] or at CO-$Pd_{iso}$ and CO-Pd-$L_1$ sites.[61,119−122] Relative to the monometallic references, the positions of the fitted components for the PdPt-MF1-com sample are slightly red-shifted, while they show a significantly lower intensity. Although a systematic calibration curve would be necessary for correlating the band intensity to the adsorbed CO concentration,[124] this difference is in line with the presence of slightly larger NM entities in the bimetallic catalyst that expose a lower number of surface sites (Pd+Pt). With three components centered around 2143, 2106, and 2100 $cm^{-1}$, the DRIFTS bands measured for the PdPt-MF1-rod catalyst almost represent the sum of the features observed for the monometallic Pt and Pd references. A similar situation was encountered for the PdPt-MF1-cub sample, although in this case, a new feature appears around 2041 $cm^{-1}$. According to the study of Hazlett *et al.*,[109] the presence of this band could indicate the formation of dicarbonyls on Pt. At the same time, this band could indicate the partial reduction of Pt sites under reaction conditions.[107,116] All in all, given the similar SNMC of the as-prepared catalysts (Table 1), the overall intensity of the CO-adsorbate bands in the pseudoabsorbance spectra showed in Figure 11c−f for the fresh catalysts aligns well with the noble metal dispersion uncovered by the complementary characterization methods used in this study, e.g., electron microscopy, and follows the order PdPt-MF1-rod ∼ PdPt-MF1-cub> PdPt-MF1-com. Most probably due to the presence of alloyed nanoparticles in the PdPt-MF2-cub sample and diminished number of exposed sites, the corresponding DRIFTS spectrum exhibits the lowest intensity among the investigated bimetallic catalysts. Moreover, the highest intensity is shown by the band centered at 2093 $cm^{-1}$ while further components are noticeable at 2124, 2063, and 2030 $cm^{-1}$, which can be assigned to coadsorption of CO and oxygen on oxidized Pt as well as to linearly bound CO at edge and corner Pt or Pd sites.[36,113,125−130]

After the CO oxidation LOff/LOut cycle to 300 °C, only small differences were observed relative to the spectral features measured for the as-prepared catalysts. A decrease in the intensity of the band around 2136 $cm^{-1}$ and an increase in those centered at 2091 and 2074 $cm^{-1}$ were noticed for the PdPt-MF1-com catalyst. A similar tendency was observed for the contributions at higher wavenumbers in the case of the


https://doi.org/10.1021/acs.jpcc.5c04366
J. Phys. Chem. C XXXX, XXX, XXX−XXX

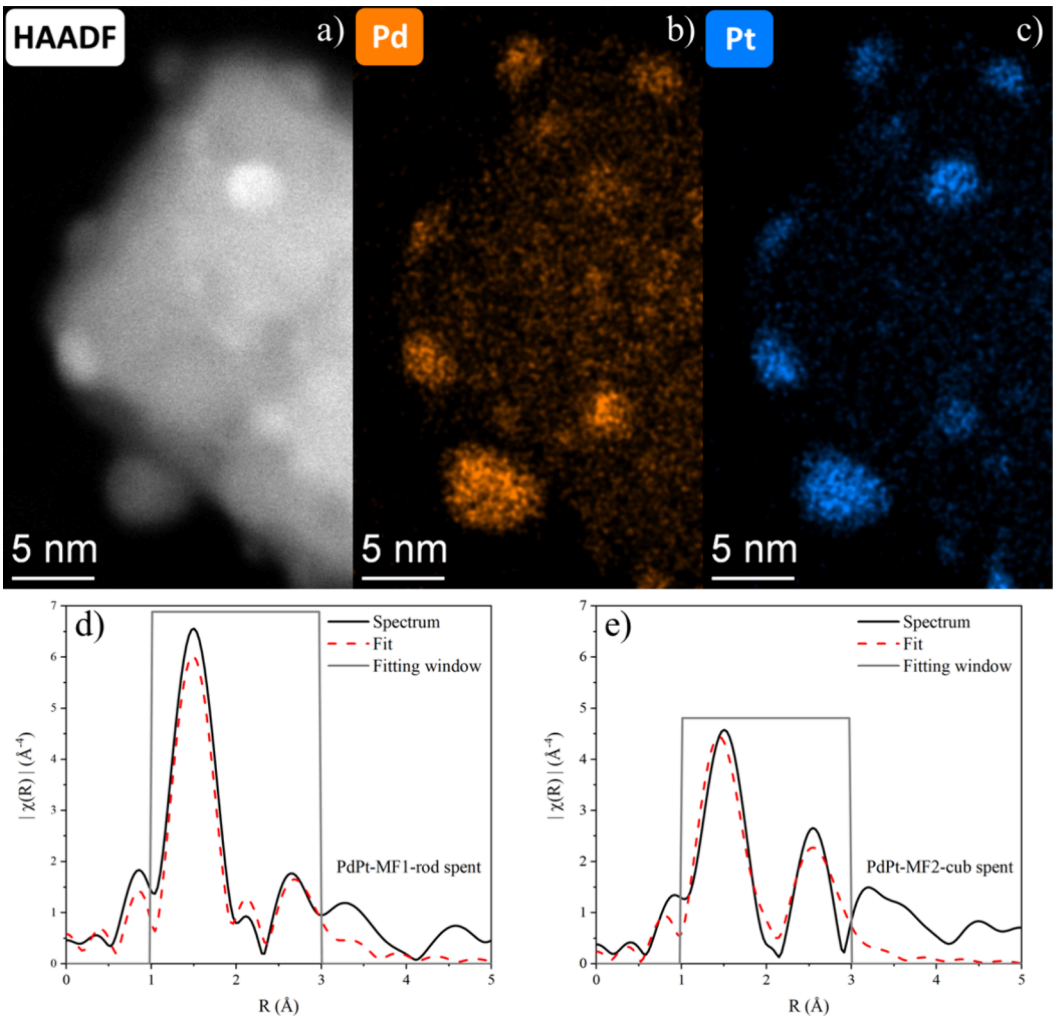


**Figure 12.** HAADF-STEM images of the spent PdPt-MF2-cub catalyst (a). EDX elemental mappings for (b) Pd and (c) Pt corresponding to the HAADF-STEM images. FT-EXAFS fitting in *R*-space at the Pd K edge for PdPt-MF1-rod spent (d) and PdPt-MF2-cub spent (e) samples.

PdPt-MF1-rod catalyst. In contrast, for PdPt-MF1-cub the contribution at 2099 $cm^{-1}$ decreases its intensity. For the catalysts containing alloyed PdPt nanoparticles, an overall increase of the pseudoabsorbance was noticed, accompanied by the appearance of more pronounced contributions toward smaller wavenumbers. This variation could be caused by partial reduction of the noble metal sites in the presence of CO.

Analogous to the monometallic catalysts, after the prereduction treatment (spectra depicted in blue in Figure 11c–f), clusters/NPs with adjacent Pd atoms are formed in all Pd–Pt bimetallic samples. This is indicated especially by the presence of CO bands below 2000 $cm^{-1}$, which were previously related to bridged carbonyls on metallic Pd species.[37,112,120,122] The most intense contribution in the DRIFTS spectra is centered around 2075 $cm^{-1}$ for the PdPt-MF1-com and PdPt-MF1-rod catalysts, and appears at ~2091 $cm^{-1}$ for the PdPt-MF1-cub sample. This region was previously assigned to linearly linked CO to partially reduced NM clusters or nanoparticles.[107,111] Although the reduction and clustering of Pt are more difficult to probe as the region of interest (2090–2000 $cm^{-1}$) is superimposed by the above-described CO-Pd-$L_1$ sites, a contribution around 2030 $cm^{-1}$ could be identified for the bimetallic catalysts. As applied for the Pt-IWI-com reference, this feature was related to the presence of reduced Pt sites. In addition to the CO adsorption sites on the noble metals, the band around 2175 $cm^{-1}$ appears after the reduction treatment and exposure to the reaction mixture (blue spectra) for the samples PdPt-MF1-rod, PdPt-MF1-cub, and PdPt-MF2-cub. Previously, this feature was correlated with CO adsorption on $Ce^{3+}$ upon partial reduction of defect sites in the vicinity of noble metal.[114,131] Important to notice is that the samples exhibiting this band are those also showing higher performance for the low temperature CO oxidation (Figure 5a).

Similarly as observed for the monometallic references, the catalysts containing homogeneously distributed Pt and Pd species with poor interaction degrees undergo reoxidation and redispersion of NM during the following LOff/LOut CO oxidation cycle. In addition to the almost complete disappearance of the CO adsorption bands at wavenumbers below 2000 $cm^{-1}$, the characteristic and poorly superimposed CO-$Pd_{iso}$ band appears for all prereduced samples in the region 2140–2120 $cm^{-1}$. Furthermore, the relative increase in the intensity of this contribution is more pronounced for PdPt-MF1-rod and PdPt-MF1-cub, confirming the stronger tendency of noble metal redispersion under lean conditions for these samples. In contrast, due to the higher stability of the alloyed PdPt nanoparticles, a broad and intense CO adsorption band is still present around 1939 $cm^{-1}$ for the PdPt-MF2-cub catalyst. This trend is in agreement with the STEM-EDX


https://doi.org/10.1021/acs.jpcc.5c04366
J. Phys. Chem. C XXXX, XXX, XXX–XXX

characterization results of the spent samples reported in Figure 7.

To further validate the difference uncovered by the DRIFTS measurements in the NM redispersion extent for the prealloyed PdPt-MF2-cub sample, STEM-EDX investigations were also performed for the spent catalyst at the end of the sixth LOff/LOut cycle. Similarly to the bimetallic catalysts containing highly dispersed species in the fresh state, the co-presence of different entities was also revealed for this spent sample. However, besides highly dispersed Pd species, the catalyst contains a high number of alloyed clusters/NPs, which seem to be preserved from the fresh catalyst state (Figures 2j–l vs 11). From the EDX quantification of several NPs, an average Pd:Pt at. ratio of 1.3 ± 0.6 was calculated, which is half of that obtained for the NPs in the fresh sample. Furthermore, EDX quantification on sample regions excluding NMNPs resulted in a Pd:Pt at. ratio of 4.7, cross-confirming the tendency of ceria nanocubes to redisperse Pd from the premixed NPs after noble metal oxidation. Nevertheless, as in the spent PdPt-MF1-cub sample (Figure 7g–i) a higher Pd dispersion was found, it appears that the competing interaction with Pt induced by the prealloying process is beneficial for the catalyst structural stability, as also indicated by the trends in the catalytic activity data.

This trend in the catalyst stability under reaction conditions was also confirmed during the evaluation of the corresponding *operando* XAS spectra collected at the beginning and end of the LOff/LOut cycles. In both PdPt-MF1-rod and PdPt-MF2-cub catalysts, the two noble metals are mostly in an oxidized state after catalyst synthesis, which included a calcination step for 1 h at 500 °C. This is indicated by the profile of the XANES spectra collected at Pd K and Pt $L_3$ edges for the fresh samples (Figure S11). Additionally, the analysis of the corresponding EXAFS region for the data obtained at the Pd K edge uncovered a pronounced contribution of the Pd–O scattering path at ∼1.47 Å in the FT-EXAFS spectra (not phase-shift corrected) for both PdPt-MF1-rod and PdPt-MF2-cub catalysts (Figure S23). The intensity of this feature is only visibly decreased at the end of the catalytic cycles for the PdPt-MF2-cub catalyst, while an additional well-defined scattering path at around 2.56 Å is noticed. Despite the highly absorbing $CeO_2$ support and low noble metal loading, which results in demanding premises for the *operando* XAS measurements, the fitting of the FT-EXAFS data at the Pd K edge was attempted for the two spent samples. A similar fitting range, comprising the first coordination shells of oxidized/metallic NM states, has been used in previous studies on Pd/$CeO_2$ monometallic catalysts.[30,119] Considering that the electron microscopy characterization revealed a highly dispersed state for the noble metal species on the surface of $CeO_2$ rods (Figure 2d–f) as well as partial NM redispersion for the PdPt-MF2-cub catalyst, the fitting was conducted by using a DFT calculated noble metal structure of $Pd^{2+}$ single sites on $CeO_2$(111), as proposed by Gashnikova *et al.*[37] Additionally, to simulate the formation of alloys or mixed oxides that were identified by electron microscopy in the PdPt-MF2-cub sample (Figures 2 and 12), the Pd–O, Pd–Pd, and Pd–Pt scattering paths were derived from adjusted Pd and PdO structures, as described in the experimental section. The results of the fitting procedure (Figures 12d,e, S24, Tables S6, and S7) indicate exclusively the presence of isolated Pd at 4-fold hollow sites on Ce in the spent PdPt-MF1-rod. In contrast, metallic Pd–Pd and Pd–Pt contributions were found, along with isolated Pd species for the spent PdPt-MF2-cub catalyst, where only partial redispersion was observed during EDXS investigations (Figure 12). This outcome suggests that the presence of alloyed Pd–Pt nanoparticles on $CeO_2$ cubes in the as-prepared sample (Figure 2) hinders the complete NM redispersion in the PdPt-MF2-cub catalyst, and improves the overall catalyst stability under reaction conditions (Figure S25). However, due to the even lower concentration of Pt in the bimetallic samples, lower edge energy, and demanding investigation conditions (capillary reactor), the complementary evaluation of the Pt $L_3$ edge operando EXAFS data could not be conducted to further corroborate the formation of Pd–Pt alloyed species. Hence, the interpretation of the EXAFS fitting results at the Pd K edge should be done with caution and only in combination with the complementary characterization data reported above, i.e., electron microscopy and *in situ* DRIFTS.

Overall, the characterization and catalytic test results obtained for the tailored prealloyed PdPt-MF2-cub sample allowed us to identify the beneficial effect of the Pd–Pt interaction on the catalyst stability under $O_2$-rich reaction conditions. While the presence of Pd–Pt alloyed nanoparticles on ceria cannot compete with the CO oxidation boost provided by the NM–$CeO_2$ interaction, the small variations in the activity of the as-prepared and prereduced PdPt-MF2-cub samples over consecutive CO LOff/LOut cycles (Figure S25) underline a higher structural stability that prevents the fast reoxidation and redispersion of both noble metals. This is particularly important for oxidation reactions that require reduced and larger nanoparticles for an active noble metal state, i.e., NO and $CH_4$ total oxidation.[22,132] In this case, also the selection of a support morphology with a low number of oxygen vacancies, i.e., $CeO_2$ cubes, could prevent a fast redispersion. However, for such cases, further thermal aging tests need to be conducted to evaluate the stability of the initial $CeO_2$ morphology and PdPt bimetallic entities during long-term operation and harsh reaction conditions. Additionally, investigations with preformed alloyed NPs with different Pd:Pt ratios are necessary to clarify the synergistic behavior of bimetallic Pd–Pt systems, as well as segregation and redispersion phenomena that are assisted by the interaction with $CeO_2$.

## 4. CONCLUSIONS

By applying elaborate catalyst preparation procedures and complementary characterization methods, two important structural features of bimetallic Pd–Pt/$CeO_2$ CO oxidation catalysts were studied: the influence of the support morphology and of the initial Pd–Pt interaction. Accordingly, two series of bimetallic Pd–Pt/$CeO_2$ samples were synthesized, aiming to highlight either the influence of the noble metal–support interplay (nanocubes, nanorods vs commercial) or of the different Pd–Pt interaction degree (on $CeO_2$-nanocubes). Microfluidic synthesis of noble metal nanoparticles allowed to control the initial Pd–Pt interaction, i.e., low or high, and the general structural uniformity in the two catalyst series. Morphologically pure and size-controlled ceria nanocubes and nanorods were obtained by hydrothermal synthesis. In contrast to analogous studies on monometallic catalysts, the surface noble metal concentration on the ceria supports was kept constant in order to decouple its effect on NM clustering/redispersion under reaction conditions. Thus, only the impact of the NM–$CeO_2$ interaction on the catalyst activity was emphasized as a function of $CeO_2$ morphology.


https://doi.org/10.1021/acs.jpcc.5c04366
J. Phys. Chem. C XXXX, XXX, XXX–XXX

The resulting samples were extensively characterized *ex situ/in situ/operando*, and compared with mono- and bimetallic catalysts supported on commercial $CeO_2$. The following main conclusions could be derived:

- A clear effect of the oxygen defect concentration on the noble metal state in the fresh catalysts, as well as on the structural evolution of Pd and Pt species under reaction conditions, was observed.
- Based on Raman spectroscopy measurements, the concentration of the oxygen vacancies was found to follow the order: $CeO_2$-nanorods > $CeO_2$-cubes > $CeO_2$-commercial. Accordingly, STEM-EDX investigations revealed that during the catalyst calcination step, highly dispersed Pd and Pt species are formed, especially on $CeO_2$-nanorods, while Pd redispersion is limited on the commercial $CeO_2$.
- The catalytic activity of the fresh bimetallic samples containing unalloyed Pt and Pd species follows the order PdPt/$CeO_2$-commercial > PdPt/$CeO_2$-cubes > PdPt/$CeO_2$-rods, which inversely correlates with the interaction strength between the two NMs and $CeO_2$. This trend is opposite to the CO oxidation activity profiles reported in literature for analogous monometallic Pt and Pd catalysts supported on $CeO_2$ nanocubes and nanorods.
- After applying a prereduction treatment at 300 °C, a higher stability in the catalytic performances during consecutive LOff/LOut CO oxidation cycles was observed for the initially unalloyed Pd−Pt/$CeO_2$ bimetallic catalysts in comparison to the monometallic counterparts. This effect was further enhanced on supports with a low oxygen defect concentration.
- Due to the contribution of the NM-$CeO_2$ perimeter sites, a higher CO oxidation activity was measured at low temperatures for the fresh unalloyed PdPt/$CeO_2$-cubes catalyst containing highly dispersed and weakly interacting Pd and Pt species compared to the corresponding sample comprising prealloyed Pd−Pt particles.
- According to the *operando* XAS and *in situ* DRIFTS investigations, the sample containing prealloyed Pd−Pt nanoparticles shows a higher structural stability during consecutive LOff/LOut CO oxidation cycles. In addition to the selection of a support with a low concentration of oxygen vacancies, this beneficial effect of Pd−Pt alloying at preventing the redispersion of the NMs on $CeO_2$ is essential for oxidation reactions that require larger NM particles for optimal performance, i.e., NO and $CH_4$ oxidation.

Overall, our study shows that by varying the number of oxygen vacancies in the $CeO_2$ support as well as the Pd−Pt interaction, the catalytic activity and stability under dynamic reaction conditions can be tuned depending on the application requirements. Considering that the NM−$CeO_2$ interplay regulates the activity and stability of such systems, the trends observed in this study for CO oxidation can serve as guidelines for the knowledge-based development of more efficient Pd−Pt/$CeO_2$ catalysts for other reactions occurring under $O_2$-rich conditions. In this regard, the selection of a specific $CeO_2$ morphology with a low or high number of oxygen vacancies is expected to promote the formation of noble metal clusters or particles or highly dispersed species, respectively, under reaction conditions. Furthermore, catalysts containing alloyed Pt−Pd particles are projected to exhibit a higher resistance toward noble metal redispersion and deactivation. All these premises need to be further evaluated for different Pd:Pt ratios, gas mixtures, and under long-term catalyst testing conditions to allow their implementation in real application conditions. Finally, additional spectroscopic investigations to probe the redox response of the perimeter ceria sites at the interface with the noble metal particles would be beneficial for obtaining a more holistic understanding of Pd−Pt/$CeO_2$-based catalysts.

## ■ ASSOCIATED CONTENT

### Data Availability Statement

The data that support the findings of this study is available on the KITopen platform at 10.35097/aqnx4ybz8n2cbe2c.

### Supporting Information

The Supporting Information is available free of charge at https://pubs.acs.org/doi/10.1021/acs.jpcc.5c04366.

Additional data and figures from catalysts characterization (i.e., XRD, STEM-EDX, SEM-EDX, Raman spectroscopy, XANES, TGA-MS, DRIFTS, EXAFS) and catalytic data (i.e., CO conversion) (PDF)

## ■ AUTHOR INFORMATION


### Corresponding Authors

**Silvia Gross** − *Institute for Chemical Technology and Polymer Chemistry (ITCP), Karlsruhe Institute of Technology (KIT), 76131 Karlsruhe, Germany; Dipartimento di Scienze Chimiche, Università degli Studi di Padova, 35131 Padova, Italy;* orcid.org/0000-0003-1860-8711; Email: silvia.gross@unipd.it

**Maria Casapu** − *Institute for Chemical Technology and Polymer Chemistry (ITCP), Karlsruhe Institute of Technology (KIT), 76131 Karlsruhe, Germany;* orcid.org/0000-0002-8755-9856; Email: maria.casapu@kit.edu

### Authors

**Andrea De Giacinto** − *Institute for Chemical Technology and Polymer Chemistry (ITCP), Karlsruhe Institute of Technology (KIT), 76131 Karlsruhe, Germany; Dipartimento di Scienze Chimiche, Università degli Studi di Padova, 35131 Padova, Italy;* orcid.org/0009-0006-6959-1381

**Paolo Dolcet** − *Institute for Chemical Technology and Polymer Chemistry (ITCP), Karlsruhe Institute of Technology (KIT), 76131 Karlsruhe, Germany; Dipartimento di Scienze Chimiche, Università degli Studi di Padova, 35131 Padova, Italy;* orcid.org/0000-0001-9583-9375

**Di Wang** − *Institute of Nanotechnology (INT), Karlsruhe Institute of Technology (KIT), 76344 Eggenstein-Leopoldshafen, Germany; Karlsruhe Nano Micro Facility (KNMFi), Karlsruhe Institute of Technology (KIT), 76344 Eggenstein-Leopoldshafen, Germany;* orcid.org/0000-0001-9817-7047

**Joachim Czechowsky** − *Institute for Chemical Technology and Polymer Chemistry (ITCP), Karlsruhe Institute of Technology (KIT), 76131 Karlsruhe, Germany;* orcid.org/0009-0000-3741-2410

**Carina B. Maliakkal** − *Institute of Nanotechnology (INT), Karlsruhe Institute of Technology (KIT), 76344 Eggenstein-Leopoldshafen, Germany*




https://doi.org/10.1021/acs.jpcc.5c04366
J. Phys. Chem. C XXXX, XXX, XXX−XXX

**Christian Kübel** − *Institute of Nanotechnology (INT), Karlsruhe Institute of Technology (KIT), 76344 Eggenstein-Leopoldshafen, Germany; Karlsruhe Nano Micro Facility (KNMFi), Karlsruhe Institute of Technology (KIT), 76344 Eggenstein-Leopoldshafen, Germany;* orcid.org/0000-0001-5701-4006

**Silke Behrens** − *Institute of Catalysis Research and Technology (IKFT), Karlsruhe Institute of Technology (KIT), 76344 Eggenstein-Leopoldshafen, Germany;* orcid.org/0000-0003-4328-9564

**Jan-Dierk Grunwaldt** − *Institute for Chemical Technology and Polymer Chemistry (ITCP), Karlsruhe Institute of Technology (KIT), 76131 Karlsruhe, Germany; Institute of Catalysis Research and Technology (IKFT), Karlsruhe Institute of Technology (KIT), 76344 Eggenstein-Leopoldshafen, Germany;* orcid.org/0000-0003-3606-0956

Complete contact information is available at: https://pubs.acs.org/10.1021/acs.jpcc.5c04366

### Author Contributions

A.D.G. conducted the study, performed most of the catalyst preparation and testing, basic and advanced characterization (XRD, Raman, TGA-MS, DRIFTS), and related data analysis, was involved in XAS experiments, and wrote the manuscript. P.D. designed and performed the XAS experiments and corresponding data evaluation, and helped during the design of the study and the discussion on the results. D.W. and C.M. performed the main TEM measurements. J.C. helped during catalyst preparation, testing, and EXAFS fitting. C.K. helped with the discussion on the TEM results. S.B., J.-D.G., and S.G. helped during the design of the study, the discussion on the results, and the paper writing. M.C. helped during the design of the study and was involved in the XAS and TGA-MS experiments, data discussion, and paper writing. All the authors commented and gave input to the manuscript.

### Notes

The authors declare no competing financial interest.

## ■ ACKNOWLEDGMENTS

This study was funded by the Deutsche Forschungsgemeinschaft (DFG, German Research Foundation)—SFB 1441—Project-ID 426888090 (projects B1, B2, B3). A.D.G. acknowledges the "Erasmus+ for Studies" which supported him with a scholarship. KIT and DFG are acknowledged for financing the Raman spectrometer (INST 121384/73-1) and the STA setup (INST 121384/70-1). This work was partly carried out with the support of the Karlsruhe Nano Micro Facility (KNMFi), a Helmholtz Research Infrastructure at KIT, within proposal 2020-024-029424. The authors acknowledge the European Synchrotron Radiation Facility (ESRF) for the provision of beamtime (proposal CH-5742) and thank C. Atzori and K. Lomachenko (BM23) for assistance. We acknowledge SOLEIL for the provision of synchrotron radiation facilities, and thank A. Zitolo, G. Alizon, and L. Barthe for assistance in using beamline SAMBA (proposal 20211613). F. Barbon (UniPD), L. Braun, and D. Gashnikova are acknowledged for help during catalyst preparation, T. Bergfeldt (IAM-AWP) for ICP-OES measurements, S. Kale and E. Barbosa for $N_2$ physisorption measurements, and S. Barth for help during DRIFTS measurements. C. Neidiger, Y. Tang, X. Huang (INT) and M. Zimmermann (IKFT) are acknowledged for support during electron microscopy measurements, and D. Doronkin, F. Tajoli (UniPD) and S.-L. Heck for support during *in situ/operando* experiments. F. Maurer helped with the design of the Table of Contents graphics. The authors thank DAPHNE4NFDI (DFG project under project number 460248799) and NFDI-consortia (NFDI4Cat, FAIRMAT, and NFDI4Chem) for fruitful discussion and valuable input for implementing FAIR data principles in this work.

## ■ REFERENCES

(1) Trovarelli, A.; Fornasiero, P. *Catalysis by Ceria and Related Materials, 2nd ed.: Vol. 12*; Catalytic Science Series; Imperial College Press, 2013; vol *12*.

(2) Sarma, B. B.; Maurer, F.; Doronkin, D. E.; Grunwaldt, J.-D. Design of Single-Atom Catalysts and Tracking Their Fate Using Operando and Advanced X-Ray Spectroscopic Tools. *Chem. Rev.* **2023**, *123* (1), 379−444.

(3) Datye, A. K.; Votsmeier, M. Opportunities and Challenges in the Development of Advanced Materials for Emission Control Catalysts. *Nat. Mater.* **2021**, *20* (8), 1049−1059.

(4) Lee, J. E.; Ok, Y. S.; Tsang, D. C. W.; Song, J.; Jung, S.-C.; Park, Y.-K. Recent Advances in Volatile Organic Compounds Abatement by Catalysis and Catalytic Hybrid Processes: A Critical Review. *Sci. Total Environ.* **2020**, *719*, No. 137405.

(5) Ding, S.; Hülsey, M. J.; Pérez-Ramírez, J.; Yan, N. Transforming Energy with Single-Atom Catalysts. *Joule* **2019**, *3* (12), 2897−2929.

(6) Melchionna, M.; Fornasiero, P. The Role of Ceria-Based Nanostructured Materials in Energy Applications. *Mater. Today* **2014**, *17* (7), 349−357.

(7) Lu, Y.; Thompson, C.; Kunwar, D.; Datye, A. K.; Karim, A. M. Origin of the High CO Oxidation Activity on $CeO_2$ Supported Pt Nanoparticles: Weaker Binding of CO or Facile Oxygen Transfer from the Support? *ChemCatChem.* **2020**, *12* (6), 1726−1733.

(8) Bernal, S.; Calvino, J. J.; Cauqui, M. A.; Gatica, J. M.; Larese, C.; Pérez Omil, J. A.; Pintado, J. M. Some Recent Results on Metal/Support Interaction Effects in NM/$CeO_2$ (NM: Noble Metal) Catalysts. *Catal. Today* **1999**, *50* (2), 175−206.

(9) Li, W.; Liu, J.; Zhao, D. Mesoporous Materials for Energy Conversion and Storage Devices. *Nat. Rev. Mater.* **2016**, *1* (6), 1−17.

(10) Yang, X.; Cheng, X.; Ma, J.; Zou, Y.; Luo, W.; Deng, Y. Large-Pore Mesoporous $CeO_2$−$ZrO_2$ Solid Solutions with In-Pore Confined Pt Nanoparticles for Enhanced CO Oxidation. *Small* **2019**, *15* (39), 1903058.

(11) Zhou, A.; Wang, J.; Wang, H.; Li, H.; Wang, J.; Shen, M. Effect of Active Oxygen on the Performance of Pt/$CeO_2$ Catalysts for CO Oxidation. *J. Rare Earths* **2018**, *36* (3), 257−264.

(12) Ferré, G.; Aouine, M.; Bosselet, F.; Burel, L.; Cadete Santos Aires, F. J.; Geantet, C.; Ntais, S.; Maurer, F.; Casapu, M.; Grunwaldt, J.-D.; et al. Exploiting the Dynamic Properties of Pt on Ceria for Low-Temperature CO Oxidation. *Catal. Sci. Technol.* **2020**, *10* (12), 3904−3917.

(13) Gänzler, A. M.; Casapu, M.; Doronkin, D. E.; Maurer, F.; Lott, P.; Glatzel, P.; Votsmeier, M.; Deutschmann, O.; Grunwaldt, J.-D. Unravelling the Different Reaction Pathways for Low Temperature CO Oxidation on Pt/$CeO_2$ and Pt/$Al_2O_3$ by Spatially Resolved Structure-Activity Correlations. *J. Phys. Chem. Lett.* **2019**, *10* (24), 7698−7705.

(14) Trovarelli, A.; Llorca, J. Ceria Catalysts at Nanoscale: How Do Crystal Shapes Shape Catalysis? *ACS Catal.* **2017**, *7* (7), 4716−4735.

(15) Gao, Y.; Wang, W.; Chang, S.; Huang, W. Morphology Effect of $CeO_2$ Support in the Preparation, Metal-Support Interaction, and Catalytic Performance of Pt/$CeO_2$ Catalysts. *ChemCatChem.* **2013**, *5* (12), 3610−3620.

(16) Gänzler, A. M.; Casapu, M.; Vernoux, P.; Loridant, S.; Cadete Santos Aires, F. J.; Epicier, T.; Betz, B.; Hoyer, R.; Grunwaldt, J.-D. Tuning the Structure of Platinum Particles on Ceria In Situ for Enhancing the Catalytic Performance of Exhaust Gas Catalysts. *Angew. Chemie - Int. Ed.* **2017**, *56* (42), 13078−13082.

(17) Casapu, M.; Fischer, A.; Gänzler, A. M.; Popescu, R.; Crone, M.; Gerthsen, D.; Türk, M.; Grunwaldt, J.-D. Origin of the Normal and Inverse Hysteresis Behavior during CO Oxidation over $Pt/Al_2O_3$. *ACS Catal.* **2017**, *7* (1), 343−355.
(18) Farmer, J. A.; Campbell, C. T. Ceria Maintains Smaller Metal Catalyst Particles by Strong Metal-Support Bonding. *Science* **2010**, *329* (5994), 933−936.
(19) Nagai, Y.; Hirabayashi, T.; Dohmae, K.; Takagi, N.; Minami, T.; Shinjoh, H.; Matsumoto, S. Sintering Inhibition Mechanism of Platinum Supported on Ceria-Based Oxide and Pt-Oxide-Support Interaction. *J. Catal.* **2006**, *242* (1), 103−109.
(20) Bruix, A.; Rodriguez, J. A.; Ramírez, P. J.; Senanayake, S. D.; Evans, J.; Park, J. B.; Stacchiola, D.; Liu, P.; Hrbek, J.; Illas, F. A New Type of Strong Metal−Support Interaction and the Production of $H_2$ through the Transformation of Water on $Pt/CeO_2$ (111) and Pt/CeOx/$TiO_2$ (110) Catalysts. *J. Am. Chem. Soc.* **2012**, *134* (21), 8968−8974.
(21) Maurer, F.; Gänzler, A.; Lott, P.; Betz, B.; Votsmeier, M.; Loridant, S.; Vernoux, P.; Murzin, V.; Bornmann, B.; Frahm, R.; et al. Spatiotemporal Investigation of the Temperature and Structure of a $Pt/CeO_2$ oxidation Catalyst for Co and Hydrocarbon Oxidation during Pulse Activation. *Ind. Eng. Chem. Res.* **2021**, *60* (18), 6662−6675.
(22) Zengel, D.; Marchuk, V.; Kurt, M.; Maurer, F.; Salcedo, A.; Michel, C.; Loffreda, D.; Aouine, M.; Loridant, S.; Vernoux, P.; et al. Pd Loading Threshold for an Efficient Noble Metal Use in $Pd/CeO_2$ Methane Oxidation Catalysts. *Appl. Catal. B Environ. Energy* **2024**, *358*, No. 124363.
(23) Zhang, Z.; Tian, J.; Lu, Y.; Yang, S.; Jiang, D.; Huang, W.; Li, Y.; Hong, J.; Hoffman, A. S.; Bare, S. R.; et al. Memory-Dictated Dynamics of Single-Atom Pt on $CeO_2$ for CO Oxidation. *Nat. Commun.* **2023**, *14* (1), 2664.
(24) Gashnikova, D.; Maurer, F.; Bauer, M. R.; Bernart, S.; Jelic, J.; Lützen, M.; Maliakkal, C. B.; Dolcet, P.; Studt, F.; Kübel, C.; et al. Lifecycle of Pd Clusters: Following the Formation and Evolution of Active Pd Clusters on Ceria During CO Oxidation by In Situ/Operando Characterization Techniques. *ACS Catal.* **2024**, *14* (19), 14871−14886.
(25) Cargnello, M.; Doan-Nguyen, V. V. T.; Gordon, T. R.; Diaz, R. E.; Stach, E. A.; Gorte, R. J.; Fornasiero, P.; Murray, C. B. Control of Metal Nanocrystal Size Reveals Metal-Support Interface Role for Ceria Catalysts. *Science* **2013**, *341* (6147), 771−773.
(26) Fan, L.; Zhang, J.; Ma, K.; Zhang, Y.; Hu, Y. M.; Kong, L.; Jia, A.; ping; Zhang, Z.; Huang, W.; Lu, J. Q. Ceria Morphology-Dependent Pd-$CeO_2$ Interaction and Catalysis in $CO_2$ Hydrogenation into Formate. *J. Catal.* **2021**, *397*, 116−127.
(27) Dong, C.; Zhou, Y.; Ta, N.; Liu, W.; Li, M.; Shen, W. Shape Impact of Nanostructured Ceria on the Dispersion of Pd Species. *Chin. J. Catal.* **2021**, *42* (12), 2234−2241.
(28) Song, B.; Choi, D.; Xin, Y.; Bowers, C. R.; Hagelin-Weaver, H. Ultra-Low Loading $Pt/CeO_2$ Catalysts: Ceria Facet Effect Affords Improved Pairwise Selectivity for Parahydrogen Enhanced NMR Spectroscopy. *Angew. Chemie - Int. Ed.* **2021**, *60* (8), 4038−4042.
(29) Song, B.; Si, S.; Soleymani, A.; Xin, Y.; Hagelin-Weaver, H. E. Effect of Ceria Surface Facet on Stability and Reactivity of Isolated Platinum Atoms. *Nano Res.* **2022**, *15* (7), 5922−5932.
(30) Spezzati, G.; Benavidez, A. D.; DeLaRiva, A. T.; Su, Y.; Hofmann, J. P.; Asahina, S.; Olivier, E. J.; Neethling, J. H.; Miller, J. T.; Datye, A. K.; et al. CO Oxidation by Pd Supported on $CeO_2$(100) and $CeO_2$(111) Facets. *Appl. Catal. B Environ.* **2019**, *243*, 36−46.
(31) Hu, Z.; Liu, X.; Meng, D.; Guo, Y.; Guo, Y.; Lu, G. Effect of Ceria Crystal Plane on the Physicochemical and Catalytic Properties of Pd/Ceria for CO and Propane Oxidation. *ACS Catal.* **2016**, *6* (4), 2265−2279.
(32) Loridant, S. Raman Spectroscopy as a Powerful Tool to Characterize Ceria-Based Catalysts. *Catal. Today* **2021**, *373*, 98−111.
(33) Lin, F.; Hoang, D. T.; Tsung, C. K.; Huang, W.; Lo, S. H. Y.; Wood, J. B.; Wang, H.; Tang, J.; Yang, P. Catalytic Properties of Pt Cluster-Decorated $CeO_2$ Nanostructures. *Nano Res.* **2011**, *4* (1), 61−71.
(34) Singhania, N.; Anumol, E. A.; Ravishankar, N.; Madras, G. Influence of $CeO_2$ Morphology on the Catalytic Activity of $CeO_2$−Pt Hybrids for CO Oxidation. *Dalt. Trans.* **2013**, *42* (43), 15343.
(35) Jones, J.; Xiong, H.; DeLaRiva, A. T.; Peterson, E. J.; Pham, H.; Challa, S. R.; Qi, G.; Oh, S.; Wiebenga, M. H.; Hernández, X. I. P.; et al. Thermally Stable Single-Atom Platinum-on-Ceria Catalysts via Atom Trapping. *Science* **2016**, *353* (6295), 150−154.
(36) Maurer, F.; Beck, A.; Jelic, J.; Wang, W.; Mangold, S.; Stehle, M.; Wang, D.; Dolcet, P.; Gänzler, A. M.; Kübel, C.; et al. Surface Noble Metal Concentration on Ceria as a Key Descriptor for Efficient Catalytic CO Oxidation. *ACS Catal.* **2022**, *12* (4), 2473−2486.
(37) Gashnikova, D.; Maurer, F.; Sauter, E.; Bernart, S.; Jelic, J.; Dolcet, P.; Maliakkal, C. B.; Wang, Y.; Wöll, C.; Studt, F.; et al. Highly Active Oxidation Catalysts through Confining Pd Clusters on $CeO_2$ Nano-Islands. *Angew. Chemie - Int. Ed.* **2024**, *63* (35), No. e202408511.
(38) Alcala, R.; DeLaRiva, A.; Peterson, E. J.; Benavidez, A.; Garcia-Vargas, C. E.; Jiang, D.; Pereira-Hernández, X. I.; Brongersma, H. H.; Veen, R.; ter; Staněk, J.; et al. Atomically Dispersed Dopants for Stabilizing Ceria Surface Area. *Appl. Catal., B* **2021**, *284*, No. 119722.
(39) Skoglundh, M.; Löwendahl, L. O.; Otterated, J. E. Combinations of Platinum and Palladium on Alumina Supports as Oxidation Catalysts. *Appl. Catal.* **1991**, *77* (1), 9−20.
(40) Carrillo, C.; Johns, T. R.; Xiong, H.; Delariva, A.; Challa, S. R.; Goeke, R. S.; Artyushkova, K.; Li, W.; Kim, C. H.; Datye, A. K. Trapping of Mobile Pt Species by PdO Nanoparticles under Oxidizing Conditions. *J. Phys. Chem. Lett.* **2014**, *5* (12), 2089−2093.
(41) Martin, N. M.; Skoglundh, M.; Smedler, G.; Raj, A.; Thompsett, D.; Velin, P.; Martinez-Casado, F. J.; Matej, Z.; Balmes, O.; Carlsson, P. A. CO Oxidation and Site Speciation for Alloyed Palladium-Platinum Model Catalysts Studied by in Situ FTIR Spectroscopy. *J. Phys. Chem. C* **2017**, *121* (47), 26321−26329.
(42) Johns, T. R.; Goeke, R. S.; Ashbacher, V.; Thüne, P. C.; Niemantsverdriet, J. W.; Kiefer, B.; Kim, C. H.; Balogh, M. P.; Datye, A. K. Relating Adatom Emission to Improved Durability of Pt−Pd Diesel Oxidation Catalysts. *J. Catal.* **2015**, *328*, 151−164.
(43) Morlang, A.; Neuhausen, U.; Klementiev, K. V.; Schütze, F. W.; Miehe, G.; Fuess, H.; Lox, E. S. Bimetallic Pt/Pd Diesel Oxidation Catalysts: Structural Characterisation and Catalytic Behaviour. *Appl. Catal. B Environ.* **2005**, *60* (3−4), 191−199.
(44) Martin, N. M.; Nilsson, J.; Skoglundh, M.; Adams, E. C.; Wang, X.; Velin, P.; Smedler, G.; Raj, A.; Thompsett, D.; Brongersma, H. H.; et al. Characterization of Surface Structure and Oxidation/Reduction Behavior of Pd-$Pt/Al_2O_3$ Model Catalysts. *J. Phys. Chem. C* **2016**, *120* (49), 28009−28020.
(45) Mussio, A.; Danielis, M.; Divins, N. J.; Llorca, J.; Colussi, S.; Trovarelli, A. Structural Evolution of Bimetallic $PtPd/CeO_2$ Methane Oxidation Catalysts Prepared by Dry Milling. *ACS Appl. Mater. Interfaces* **2021**, *13* (27), 31614−31623.
(46) Nassiri, H.; Lee, K.; Hu, Y.; Hayes, R. E.; Scott, R. W. J.; Semagina, N. Platinum Inhibits Low-Temperature Dry Lean Methane Combustion through Palladium Reduction in Pd−$Pt/Al_2O_3$: An In Situ X-ray Absorption Study. *ChemPhysChem* **2017**, *18* (2), 238−244.
(47) Nassiri, H.; Lee, K.-E.; Hu, Y.; Hayes, R. E.; Scott, R. W. J.; Semagina, N. Water Shifts PdO-Catalyzed Lean Methane Combustion to Pt-Catalyzed Rich Combustion in Pd−Pt Catalysts: In Situ X-Ray Absorption Spectroscopy. *J. Catal.* **2017**, *352*, 649−656.
(48) Mai, H. X.; Sun, L. D.; Zhang, Y. W.; Si, R.; Feng, W.; Zhang, H. P.; Liu, H. C.; Yan, C. H. Shape-Selective Synthesis and Oxygen Storage Behavior of Ceria Nanopolyhedra, Nanorods, and Nanocubes. *J. Phys. Chem. B* **2005**, *109* (51), 24380−24385.
(49) Lyu, G. M.; Wang, Y. J.; Huang, X.; Zhang, H. Y.; Sun, L. D.; Liu, Y. J.; Yan, C. H. Hydrophilic $CeO_2$ Nanocubes Protect Pancreatic $\beta$-Cell Line INS-1 from H2O2-Induced Oxidative Stress. *Nanoscale* **2016**, *8* (15), 7923−7932.


https://doi.org/10.1021/acs.jpcc.5c04366
J. Phys. Chem. C XXXX, XXX, XXX−XXX

(50) Sharapa, D. I.; Doronkin, D. E.; Studt, F.; Grunwaldt, J.-D.; Behrens, S. Moving Frontiers in Transition Metal Catalysis: Synthesis, Characterization and Modeling. *Adv. Mater.* **2019**, *31* (26), 1807381.
(51) Tofighi, G.; Lichtenberg, H.; Pesek, J.; Sheppard, T. L.; Wang, W.; Schöttner, L.; Rinke, G.; Dittmeyer, R.; Grunwaldt, J.-D. Continuous Microfluidic Synthesis of Colloidal Ultrasmall Gold Nanoparticles:: In Situ Study of the Early Reaction Stages and Application for Catalysis. *React. Chem. Eng.* **2017**, *2* (6), 876−884.
(52) Tofighi, G.; Gaur, A.; Doronkin, D. E.; Lichtenberg, H.; Wang, W.; Wang, D.; Rinke, G.; Ewinger, A.; Dittmeyer, R.; Grunwaldt, J.-D. Microfluidic Synthesis of Ultrasmall AuPd Nanoparticles with a Homogeneously Mixed Alloy Structure in Fast Continuous Flow for Catalytic Applications. *J. Phys. Chem. C* **2018**, *122* (3), 1721−1731.
(53) Venediktov, A. B.; Korenev, S. V.; Vasil'chenko, D. B.; Zadesenets, A. V.; Filatov, E. Y.; Mamonov, S. N.; Ivanova, L. V.; Prudnikova, N. G.; Semitut, E. Y. On Preparation of Platinum(IV) Nitrate Solutions from Hexahydroxoplatinates(IV). *Russ. J. Appl. Chem.* **2012**, *85* (7), 995−1002.
(54) Vasilchenko, D.; Tkachev, S.; Baidina, I.; Korenev, S. Speciation of Platinum(IV) in Nitric Acid Solutions. *Inorg. Chem.* **2013**, *52* (18), 10532−10541.
(55) Montagne, L.; Grunwaldt, J.-D.; Kleist, W.; Xuhong, M.; Min, S.; Xiaomei, J.; Junwen, S.; Heyte, S.; Froidevaux, R.; Schneider, M.; Dumeignil, F.; Cooper, A. I.; Nichols, R. J.; Creeth, A.; Davies, H.; Higgins, S.; Alston, B. Global Challenges in Chemicals and Energies - Standardization and Acceleration of Catalysis R & D. In *Modern Applications of High Throughput R&D in Heterogeneous Catalysis*; BENTHAM SCIENCE PUBLISHERS, 2014; pp 310−316.
(56) Molinet-Chinaglia, C.; Piccolo, L.; Loridant, S. Investigating the Dynamics of Pt/$CeO_2$ Catalysts at the Powder Agglomerate Scale by Combining In Situ Hyperspectral Raman Imaging and SEM-EDX Analysis. *ChemCatChem.* **2023**, *15* (19), No. e202300627.
(57) Pereira-Hernández, X. I.; DeLaRiva, A.; Muravev, V.; Kunwar, D.; Xiong, H.; Sudduth, B.; Engelhard, M.; Kovarik, L.; Hensen, E. J. M.; Wang, Y.; et al. Tuning Pt-$CeO_2$ Interactions by High-Temperature Vapor-Phase Synthesis for Improved Reducibility of Lattice Oxygen. *Nat. Commun.* **2019**, *10*, 1358.
(58) Brunauer, S.; Emmett, P. H.; Teller, E. Adsorption of Gases in Multimolecular Layers. *J. Am. Chem. Soc.* **1938**, *60* (2), 309−319.
(59) Barrett, E. P.; Joyner, L. G.; Halenda, P. P. The Determination of Pore Volume and Area Distributions in Porous Substances. I. Computations from Nitrogen Isotherms. *J. Am. Chem. Soc.* **1951**, *73* (1), 373−380.
(60) Lee, Y.; He, G.; Akey, A. J.; Si, R.; Flytzani-Stephanopoulos, M.; Herman, I. P. Raman Analysis of Mode Softening in Nanoparticle $CeO_{2-\delta}$ and Au-$CeO_{2-\delta}$ during CO Oxidation. *J. Am. Chem. Soc.* **2011**, *133* (33), 12952−12955.
(61) Sarma, B. B.; Jelic, J.; Neukum, D.; Doronkin, D. E.; Huang, X.; Bernart, S.; Studt, F.; Grunwaldt, J.-D. Tracking and Understanding Dynamics of Atoms and Clusters of Late Transition Metals with In-Situ DRIFT and XAS Spectroscopy Assisted by DFT. *J. Phys. Chem. C* **2023**, *127* (23), 11419−11419.
(62) Maurer, F.; Jelic, J.; Wang, J.; Gänzler, A.; Dolcet, P.; Wöll, C.; Wang, Y.; Studt, F.; Casapu, M.; Grunwaldt, J.-D. Tracking the Formation, Fate and Consequence for Catalytic Activity of Pt Single Sites on $CeO_2$. *Nat. Catal.* **2020**, *3* (10), 824−833.
(63) Rosa, A. D.; Garbarino, G.; Rodrigues, J. E.; Mijit, E.; Jacobs, J.; Bugnazet, D.; Pasternak, S.; Berruyer, G.; Moyne, A.; Clavel, C.; et al. New Opportunities for High Pressure X-Ray Absorption Spectroscopy at ID24-DCM and BM23 with the Extremely Brilliant Source of the ESRF. *High Press. Res.* **2024**, *44* (3), 248−276.
(64) Briois, V.; Fonda, E.; Belin, S.; Barthe, L.; La Fontaine, C.; Langlois, F.; Ribbens, M.; Villain, F. SAMBA: The 4−40 KeV X-Ray Absorption Spectroscopy Beamline at SOLEIL. In *UVX 2010; EDP Sciences: Les Ulis*; EDP: France, 2011; pp 41−47.
(65) Grunwaldt, J. D.; Caravati, M.; Hannemann, S.; Baiker, A. X-Ray Absorption Spectroscopy under Reaction Conditions: Suitability of Different Reaction Cells for Combined Catalyst Characterization and Time-Resolved Studies. *Phys. Chem. Chem. Phys.* **2004**, *6* (11), 3037−3047.
(66) Ravel, B.; Newville, M. ATHENA, ARTEMIS, HEPHAESTUS: Data Analysis for X-Ray Absorption Spectroscopy Using IFEFFIT. *J. Synchrotron Radiat.* **2005**, *12* (4), 537−541.
(67) Bugaev, A. L.; Guda, A. A.; Lazzarini, A.; Lomachenko, K. A.; Groppo, E.; Pellegrini, R.; Piovano, A.; Emerich, H.; Soldatov, A. V.; Bugaev, L. A.; et al. In Situ Formation of Hydrides and Carbides in Palladium Catalyst: When XANES Is Better than EXAFS and XRD. *Catal. Today* **2017**, *283*, 119−126.
(68) Langford, J. I.; Wilson, A. J. C. Scherrer after Sixty Years: A Survey and Some New Results in the Determination of Crystallite Size. *J. Appl. Crystallogr.* **1978**, *11* (2), 102−113.
(69) Florea, I.; Feral-Martin, C.; Majimel, J.; Ihiawakrim, D.; Hirlimann, C.; Ersen, O. Three-Dimensional Tomographic Analyses of $CeO_2$ Nanoparticles. *Cryst. Growth Des.* **2013**, *13* (3), 1110−1121.
(70) Yan, L.; Yu, R.; Chen, J.; Xing, X. Template-Free Hydrothermal Synthesis of $CeO_2$ Nano-Octahedrons and Nanorods: Investigation of the Morphology Evolution. *Cryst. Growth Des.* **2008**, *8* (5), 1474−1477.
(71) Agarwal, S.; Lefferts, L.; Mojet, B. L.; Ligthart, D. A. J. M.; Hensen, E. J. M.; Mitchell, D. R. G.; Erasmus, W. J.; Anderson, B. G.; Olivier, E. J.; Neethling, J. H.; et al. Exposed Surfaces on Shape-Controlled Ceria Nanoparticles Revealed through AC-TEM and Water-Gas Shift Reactivity. *ChemSusChem* **2013**, *6* (10), 1898−1906.
(72) Torrente-Murciano, L.; Gilbank, A.; Puertolas, B.; Garcia, T.; Solsona, B.; Chadwick, D. Shape-Dependency Activity of Nano-structured $CeO_2$ in the Total Oxidation of Polycyclic Aromatic Hydrocarbons. *Appl. Catal. B Environ.* **2013**, *132*−*133*, 116−122.
(73) Toshima, N.; Yonezawa, T. Bimetallic Nanoparticles—Novel Materials for Chemical and Physical Applications. *New J. Chem.* **1998**, *22* (11), 1179−1201.
(74) Alexeev, O. S.; Siani, A.; Lafaye, G.; Williams, C. T.; Ploehn, H. J.; Amiridis, M. D. EXAFS Characterization of Dendrimer-Pt Nanocomposites Used for the Preparation of Pt/$\gamma$-$Al_2O_3$ Catalysts. *J. Phys. Chem. B* **2006**, *110* (49), 24903−24914.
(75) Ozturk, O.; Black, T. J.; Perrine, K.; Pizzolato, K.; Williams, C. T.; Parsons, F. W.; Ratliff, J. S.; Gao, J.; Murphy, C. J.; Xie, H.; et al. Thermal Decomposition of Generation-4 Polyamidoamine Dendrimer Films: Decomposition Catalyzed by Dendrimer-Encapsulated Pt Particles. *Langmuir* **2005**, *21* (9), 3998−4006.
(76) Knecht, M. R.; Weir, M. G.; Myers, V. S.; Pyrz, W. D.; Ye, H.; Petkov, V.; Buttrey, D. J.; Frenkel, A. I.; Crooks, R. M. Synthesis and Characterization of Pt Dendrimer-Encapsulated Nanoparticles: Effect of the Template on Nanoparticle Formation. *Chem. Mater.* **2008**, *20* (16), 5218−5228.
(77) Ge, S.; Chen, Y.; Tang, X.; Shen, Y.; Lou, Y.; Wang, L.; Guo, Y.; Llorca, J. Preformed Pt Nanoparticles Supported on Nanoshaped $CeO_2$ for Total Propane Oxidation. *ACS Appl. Nano Mater.* **2023**, *6* (16), 15073−15084.
(78) Eliasson, H.; Niu, Y.; Palmer, R. E.; Grönbeck, H.; Erni, R. Support-Facet-Dependent Morphology of Small Pt Particles on Ceria. *Nanoscale* **2023**, *15* (47), 19091−19098.
(79) Sartoretti, E.; Novara, C.; Giorgis, F.; Piumetti, M.; Bensaid, S.; Russo, N.; Fino, D. In Situ Raman Analyses of the Soot Oxidation Reaction over Nanostructured Ceria-Based Catalysts. *Sci. Rep.* **2019**, *9*, 3875.
(80) McBride, J. R.; Hass, K. C.; Poindexter, B. D.; Weber, W. H. Raman and X-Ray Studies of $Ce_{1-X}RE_XO_{2-Y}$, Where RE = La, Pr, Nd, Eu, Gd, and Tb. *J. Appl. Phys.* **1994**, *76* (4), 2435−2441.
(81) Weber, W. H.; Hass, K. C.; McBride, J. R. Raman Study of $CeO_2$: Second-Order Scattering, Lattice Dynamics, and Particle-Size Effects. *Phys. Rev. B* **1993**, *48* (1), 178−185.
(82) Daniel, M.; Loridant, S. Probing Reoxidation Sites by in Situ Raman Spectroscopy: Differences between Reduced $CeO_2$ and Pt/$CeO_2$. *J. Raman Spectrosc.* **2012**, *43* (9), 1312−1319.
(83) Wu, Z.; Li, M.; Howe, J.; Meyer, H. M.; Overbury, S. H. Probing Defect Sites on $CeO_2$ Nanocrystals with Well-Defined


https://doi.org/10.1021/acs.jpcc.5c04366
J. Phys. Chem. C XXXX, XXX, XXX−XXX

Surface Planes by Raman Spectroscopy and $O_2$ Adsorption. *Langmuir* **2010**, *26* (21), 16595−16606.
(84) Taniguchi, T.; Watanabe, T.; Sugiyama, N.; Subramani, A. K.; Wagata, H.; Matsushita, N.; Yoshimura, M. Identifying Defects in Ceria-Based Nanocrystals by UV Resonance Raman Spectroscopy. *J. Phys. Chem. C* **2009**, *113* (46), 19789−19793.
(85) Li, L.; Chen, F.; Lu, J. Q.; Luo, M. F. Study of Defect Sites in $Ce_{1-x}M_xO_{2-\delta}$ (x = 0.2) Solid Solutions Using Raman Spectroscopy. *J. Phys. Chem. A* **2011**, *115* (27), 7972−7977.
(86) Conesa, J. C. Computer Modeling of Surfaces and Defects on Cerium Dioxide. *Surf. Sci.* **1995**, *339* (3), 337−352.
(87) Nolan, M.; Grigoleit, S.; Sayle, D. C.; Parker, S. C.; Watson, G. W. Density Functional Theory Studies of the Structure and Electronic Structure of Pure and Defective Low Index Surfaces of Ceria. *Surf. Sci.* **2005**, *576* (1−3), 217−229.
(88) Branda, M. M.; Ferullo, R. M.; Causá, M.; Illas, F. Relative Stabilities of Low Index and Stepped $CeO_2$ Surfaces from Hybrid and GGA + U Implementations of Density Functional Theory. *J. Phys. Chem. C* **2011**, *115* (9), 3716−3721.
(89) Nolan, M.; Parker, S. C.; Watson, G. W. The Electronic Structure of Oxygen Vacancy Defects at the Low Index Surfaces of Ceria. *Surf. Sci.* **2005**, *595* (1−3), 223−232.
(90) Schilling, C.; Hofmann, A.; Hess, C.; Ganduglia-Pirovano, M. V. Raman Spectra of Polycrystalline $CeO_2$: A Density Functional Theory Study. *J. Phys. Chem. C* **2017**, *121* (38), 20834−20849.
(91) Artiglia, L.; Orlando, F.; Roy, K.; Kopelent, R.; Safonova, O.; Nachtegaal, M.; Huthwelker, T.; van Bokhoven, J. A. Introducing Time Resolution to Detect $Ce^{3+}$ Catalytically Active Sites at the Pt/$CeO_2$ Interface through Ambient Pressure X-Ray Photoelectron Spectroscopy. *J. Phys. Chem. Lett.* **2017**, *8* (1), 102−108.
(92) Kopelent, R.; Van Bokhoven, J. A.; Nachtegaal, M.; Szlachetko, J.; Safonova, O. V. X-Ray Emission Spectroscopy: Highly Sensitive Techniques for Time-Resolved Probing of Cerium Reactivity under Catalytic Conditions. *Phys. Chem. Chem. Phys.* **2016**, *18* (47), 32486−32493.
(93) Stadnichenko, A. I.; Slavinskaya, E. M.; Stonkus, O. A.; Boronin, A. I. Low-Temperature CO Oxidation by the Pt/$CeO_2$ Based Catalysts. *ChemCatChem.* **2024**, *16* (15), No. e202301727.
(94) McBride, J. R.; Hass, K. C.; Weber, W. H. Resonance-Raman and Lattice-Dynamics Studies of Single-Crystal PdO. *Phys. Rev. B* **1991**, *44* (10), 5016−5028.
(95) Zhang, L.; Chen, R.; Tu, Y.; Gong, X.; Cao, X.; Xu, Q.; Li, Y.; Ye, B.; Ye, Y.; Zhu, J. Revealing the Crystal Facet Effect of Ceria in Pd/$CeO_2$ Catalysts toward the Selective Oxidation of Benzyl Alcohol. *ACS Catal.* **2023**, *13* (4), 2202−2213.
(96) Lee, J.; Ryou, Y.; Chan, X.; Kim, T. J.; Kim, D. H. How Pt Interacts with $CeO_2$ under the Reducing and Oxidizing Environments at Elevated Temperature: The Origin of Improved Thermal Stability of Pt/$CeO_2$ Compared to $CeO_2$. *J. Phys. Chem. C* **2016**, *120* (45), 25870−25879.
(97) Lin, W.; Herzing, A. A.; Kiely, C. J.; Wachs, I. E. Probing Metal-Support Interactions under Oxidizing and Reducing Conditions: In Situ Raman and Infrared Spectroscopic and Scanning Transmission Electron Microscopic-X-Ray Energy-Dispersive Spectroscopic Investigation of Supported Platinum Catalysts. *J. Phys. Chem. C* **2008**, *112* (15), 5942−5951.
(98) Brogan, M. S.; Dines, T. J.; Cairns, J. A. Raman Spectroscopic Study of the Pt-$CeO_2$ Interaction in the Pt/$Al_2O_3$-$CeO_2$ Catalyst. *J. Chem. Soc. Faraday Trans.* **1994**, *90* (10), 1461−1466.
(99) Colussi, S.; Gayen, A.; Camellone, M. F.; Boaro, M.; Llorca, J.; Fabris, S.; Trovarelli, A. Nanofaceted Pd-O Sites in Pd-Ce Surface Superstructures: Enhanced Activity in Catalytic Combustion of Methane. *Angew. Chem., Int. Ed.* **2009**, *48* (45), 8481−8484.
(100) Gänzler, A. M.; Casapu, M.; Maurer, F.; Störmer, H.; Gerthsen, D.; Ferré, G.; Vernoux, P.; Bornmann, B.; Frahm, R.; Murzin, V.; et al. Tuning the Pt/$CeO_2$ Interface by in Situ Variation of the Pt Particle Size. *ACS Catal.* **2018**, *8* (6), 4800−4811.
(101) Dolcet, P.; Maurer, F.; Casapu, M.; Grunwaldt, J.-D. Insights into the Structural Dynamics of Pt/$CeO_2$ Single-Site Catalysts during CO Oxidation. *Catalysts* **2021**, *11* (5), 617.
(102) Soubaihi, R. M.; Al; Saoud, K. M.; Dutta, J. Critical Review of Low-Temperature CO Oxidation and Hysteresis Phenomenon on Heterogeneous Catalysts. *Catalysts* **2018**, *8* (12), 660.
(103) Dubbe, H.; Bühner, F.; Eigenberger, G.; Nieken, U. Hysteresis Phenomena on Platinum and Palladium-Based Diesel Oxidation Catalysts (DOCs). *Emiss. Control Sci. Technol.* **2016**, *2* (3), 137−144.
(104) Goodman, E. D.; Dai, S.; Yang, A. C.; Wrasman, C. J.; Gallo, A.; Bare, S. R.; Hoffman, A. S.; Jaramillo, T. F.; Graham, G. W.; Pan, X.; et al. Uniform Pt/Pd Bimetallic Nanocrystals Demonstrate Platinum Effect on Palladium Methane Combustion Activity and Stability. *ACS Catal.* **2017**, *7* (7), 4372−4380.
(105) Persson, K.; Ersson, A.; Colussi, S.; Trovarelli, A.; Järås, S. G. Catalytic Combustion of Methane over Bimetallic Pd−Pt Catalysts: The Influence of Support Materials. *Appl. Catal. B Environ.* **2006**, *66* (3−4), 175−185.
(106) He, J.; Yang, X.; Zhu, Z.; Luo, X.; Wu, C.; Cui, Y.; Ge, Q.; Qiu, J.; Xu, L.; Chen, M. Enhanced Low-Temperature CO Oxidation Activity through Crystal Facet Engineering of Pd/CeO2 Catalysts. *Ceram. Int.* **2024**, *50* (19), 36363−36374.
(107) Gänzler, A. M.; Betz, B.; Baier-Stegmaier, S.; Belin, S.; Briois, V.; Votsmeier, M.; Casapu, M. Operando X-Ray Absorption Spectroscopy Study During Conditioning of Pt-Based Catalysts and Its Implications for CO Oxidation. *J. Phys. Chem. C* **2020**, *124* (37), 20090−20100.
(108) Ho, P. H.; Woo, J. W.; Ilmasani, R. F.; Han, J.; Olsson, L. The Role of Pd-Pt Interactions in the Oxidation and Sulfur Resistance of Bimetallic Pd-Pt/$\gamma$-$Al_2O_3$ Diesel Oxidation Catalysts. *Ind. Eng. Chem. Res.* **2021**, *60* (18), 6596−6612.
(109) Hazlett, M. J.; Moses-Debusk, M.; Parks, J. E.; Allard, L. F.; Epling, W. S. Kinetic and Mechanistic Study of Bimetallic Pt-Pd/$Al_2O_3$ Catalysts for CO and $C_3H_6$ Oxidation. *Appl. Catal. B Environ.* **2017**, *202*, 404−417.
(110) Kaya, S.; Erunal, E.; Shaltaf, R.; Ellialtioğlu, Ş.; Uner, D. On the Structure Sensitivity of CO Oxidation on Alumina Supported Pd-Pt Bimetallic Catalysts. *Turkish J. Chem.* **2009**, *33* (1), 11−21.
(111) Salcedo, A.; Zengel, D.; Maurer, F.; Casapu, M.; Grunwaldt, J.-D.; Michel, C.; Loffreda, D. Identifying the Structure of Supported Metal Catalysts Using Vibrational Fingerprints from Ab Initio Nanoscale Models. *Small* **2023**, *19* (34), 2300945.
(112) Meunier, F. C. Relevance of IR Spectroscopy of Adsorbed CO for the Characterization of Heterogeneous Catalysts Containing Isolated Atoms. *J. Phys. Chem. C* **2021**, *125* (40), 21810−21823.
(113) Bazin, P.; Saur, O.; Lavalley, J. C.; Daturi, M.; Blanchard, G. FT-IR Study of CO Adsorption on Pt/$CeO_2$: Characterisation and Structural Rearrangement of Small Pt Particles. *Phys. Chem. Chem. Phys.* **2005**, *7* (1), 187−194.
(114) Wang, J.; Sauter, E.; Nefedov, A.; Heißler, S.; Maurer, F.; Casapu, M.; Grunwaldt, J.-D.; Wang, Y.; Wöll, C. Dynamic Structural Evolution of Ceria-Supported Pt Particles: A Thorough Spectroscopic Study. *J. Phys. Chem. C* **2022**, *126* (21), 9051−9058.
(115) Liu, Q.; Yang, P.; Tan, W.; Yu, H.; Ji, J.; Wu, C.; Cai, Y.; Xie, S.; Liu, F.; Hong, S.; et al. Fabricating Robust Pt Clusters on Sn-Doped $CeO_2$ for CO Oxidation: A Deep Insight into Support Engineering and Surface Structural Evolution. *Chem. − Eur. J.* **2023**, *29* (16), No. e202203432.
(116) Resasco, J.; DeRita, L.; Dai, S.; Chada, J. P.; Xu, M.; Yan, X.; Finzel, J.; Hanukovich, S.; Hoffman, A. S.; Graham, G. W.; et al. Uniformity Is Key in Defining Structure−Function Relationships for Atomically Dispersed Metal Catalysts: The Case of Pt/$CeO_2$. *J. Am. Chem. Soc.* **2020**, *142* (1), 169−184.
(117) Liu, X.; Jia, S.; Yang, M.; Tang, Y.; Wen, Y.; Chu, S.; Wang, J.; Shan, B.; Chen, R. Activation of Subnanometric Pt on Cu-Modified $CeO_2$ via Redox-Coupled Atomic Layer Deposition for CO Oxidation. *Nat. Commun.* **2020**, *11* (1), 4240.
(118) Spezzati, G.; Su, Y.; Hofmann, J. P.; Benavidez, A. D.; DeLaRiva, A. T.; McCabe, J.; Datye, A. K.; Hensen, E. J. M.


https://doi.org/10.1021/acs.jpcc.5c04366
J. Phys. Chem. C XXXX, XXX, XXX−XXX

Atomically Dispersed Pd-O Species on $CeO_2$ (111) as Highly Active Sites for Low-Temperature CO Oxidation. *ACS Catal.* **2017**, *7* (10), 6887−6891.
(119) Muravev, V.; Spezzati, G.; Su, Y. Q.; Parastaev, A.; Chiang, F. K.; Longo, A.; Escudero, C.; Kosinov, N.; Hensen, E. J. M. Interface Dynamics of Pd−$CeO_2$ Single-Atom Catalysts during CO Oxidation. *Nat. Catal.* **2021**, *4* (6), 469−478.
(120) Muravev, V.; Simons, J. F. M.; Parastaev, A.; Verheijen, M. A.; Struijs, J. J. C.; Kosinov, N.; Hensen, E. J. M. Operando Spectroscopy Unveils the Catalytic Role of Different Palladium Oxidation States in CO Oxidation on Pd/$CeO_2$ Catalysts. *Angew. Chemie Int. Ed.* **2022**, *61* (23), No. e202200434.
(121) Jiang, D.; Wan, G.; García-Vargas, C. E.; Li, L.; Pereira-Hernández, X. I.; Wang, C.; Wang, Y. Elucidation of the Active Sites in Single-Atom $Pd_1/CeO_2$ Catalysts for Low-Temperature CO Oxidation. *ACS Catal.* **2020**, *10* (19), 11356−11364.
(122) Tereshchenko, A.; Guda, A.; Polyakov, V.; Rusalev, Y.; Butova, V.; Soldatov, A. Pd Nanoparticle Growth Monitored by DRIFT Spectroscopy of Adsorbed CO. *Analyst* **2020**, *145* (23), 7534−7540.
(123) Grill, C. M.; Gonzalez, R. D. Infrared Study of the Adsorption of CO and NO on Silica-Supported Pd and Pt-Pd. *J. Phys. Chem.* **1980**, *84* (8), 878−882.
(124) Sirita, J.; Phanichphant, S.; Meunier, F. C. Quantitative Analysis of Adsorbate Concentrations by Diffuse Reflectance FT-IR. *Anal. Chem.* **2007**, *79* (10), 3912−3918.
(125) Boubnov, A.; Gänzler, A.; Conrad, S.; Casapu, M.; Grunwaldt, J.-D. Oscillatory CO Oxidation over Pt/$Al_2O_3$ Catalysts Studied by in Situ XAS and DRIFTS. *Top. Catal.* **2013**, *56* (1−8), 333−338.
(126) Kaftan, A.; Kollhoff, F.; Nguyen, T.-S.; Piccolo, L.; Laurin, M.; Libuda, J. Sensitivity of CO Oxidation toward Metal Oxidation State in Ceria-Supported Catalysts: An Operando DRIFTS-MS Study. *Catal. Sci. Technol.* **2016**, *6* (3), 818−828.
(127) Krasser, W.; Fadini, A.; Renouprez, A. The Vibrational Spectra of Chemisorbed Carbon Monoxide and Ethylene. *J. Mol. Struct.* **1980**, *60* (C), 427−430.
(128) Ke, J.; Zhu, W.; Jiang, Y.; Si, R.; Wang, Y.-J.; Li, S.-C.; Jin, C.; Liu, H.; Song, W.-G.; Yan, C.-H.; et al. Strong Local Coordination Structure Effects on Subnanometer $PtO_X$ Clusters over $CeO_2$ Nanowires Probed by Low-Temperature CO Oxidation. *ACS Catal.* **2015**, *5* (9), 5164−5173.
(129) Aleksandrov, H. A.; Neyman, K. M.; Hadjiivanov, K. I.; Vayssilov, G. N. Can the State of Platinum Species Be Unambiguously Determined by the Stretching Frequency of an Adsorbed CO Probe Molecule? *Phys. Chem. Chem. Phys.* **2016**, *18* (32), 22108−22121.
(130) Gänzler, A. M.; Lichtenberg, H.; Frenkel, A. I.; Casapu, M.; Boubnov, A.; Wang, D.; Grunwaldt, J.-D. Using Combined XAS/DRIFTS to Study CO/NO Oxidation over Pt/$Al_2O_3$ Catalysts. *J. Phys. Conf. Ser.* **2016**, *712* (1), No. 012045.
(131) Yang, C.; Wöll, C. Infrared Reflection-Absorption Spectroscopy (IRRAS) Applied to Oxides: Ceria as a Case Study. *Surf. Sci.* **2024**, *749*, No. 122550.
(132) Boubnov, A.; Dahl, S.; Johnson, E.; Molina, A. P.; Simonsen, S. B.; Cano, F. M.; Helveg, S.; Lemus-Yegres, L. J.; Grunwaldt, J.-D. Structure-Activity Relationships of Pt/$Al_2O_3$ Catalysts for CO and NO Oxidation at Diesel Exhaust Conditions. *Appl. Catal. B Environ.* **2012**, *126*, 315−325.




https://doi.org/10.1021/acs.jpcc.5c04366
J. Phys. Chem. C XXXX, XXX, XXX−XXX